Use of Cloud Model Microphysics for Passive Microwave-Based Precipitation Retrieval: Significance of Consistency between Model and Measurement Manifolds

GIULIA PANEGROSSI,*,+ STEFANO DIETRICH,*,+ FRANK S. MARZANO,# ALBERTO MUGNAI,*
ERIC A. SMITH,@ XUWU XIANG,@ GREGORY J. TRIPOLI,& PAO K. WANG,& AND
J. P. V. POIARES BAPTISTA**

* *Istituto di Fisica dell'Atmosfera/CNR, Frascati, Italy*
+ *Fondazione per la Meteorologia Applicata, Florence, Italy*
# *Dipartimento di Ingegneria Elettronica, University of Rome, La Sapienza, Rome, Italy*
@ *Department of Meteorology, The Florida State University, Tallahassee, Florida*
& *Department of Atmospheric and Oceanic Sciences, University of Wisconsin–Madison, Madison, Wisconsin*
** *ESA/ESTEC, Noordwijk, the Netherlands*

(Manuscript received 5 March 1996, in final form 30 December 1996)

ABSTRACT

Precipitation estimation from passive microwave radiometry based on physically based profile retrieval algorithms must be aided by a microphysical generator providing structure information on the lower portions of the cloud, consistent with the upper-cloud structures that are sensed. One of the sources for this information is mesoscale model simulations involving explicit or parameterized microphysics. Such microphysical information can be then associated to brightness temperature signatures by using radiative transfer models, forming what are referred to as cloud–radiation databases. In this study cloud–radiation databases from three different storm simulations involving two different mesoscale models run at cloud scales are developed and analyzed. Each database relates a set of microphysical profile realizations describing the space–time properties of a given precipitating storm to multifrequency brightness temperatures associated to a measuring radiometer. In calculating the multifrequency signatures associated with the individual microphysical profiles over model space–time, the authors form what are called brightness temperature model manifolds. Their dimensionality is determined by the number of frequencies carried by the measuring radiometer. By then forming an analogous measurement manifold based on the actual radiometer observations, the radiative consistency between the model representation of a rain cloud and the measured representation are compared. In the analysis, the authors explore how various microphysical, macrophysical, and environmental factors affect the nature of the model manifolds, and how these factors produce or mitigate mismatch between the measurement and model manifolds. Various methods are examined that can be used to eliminate such mismatch. The various cloud–radiation databases are also used with a simplified profile retrieval algorithm to examine the sensitivity of the retrieved hydrometeor profiles and surface rainrates to the different microphysical, macrophysical, and environmental factors of the simulated storms. The results emphasize the need for physical retrieval algorithms to account for a number of these factors, thus preventing biased interpretation of the rain properties of precipitating storms, and minimizing rms uncertainties in the retrieved quantities.

1. Introduction

Physically based algorithms for precipitation profile retrieval from passive microwave satellite measurements use precipitating cloud–radiation databases that can be derived from cloud model simulations or from radar measurements, or from a combination of them (Mugnai et al. 1993; Smith et al. 1994a; Wilheit et al. 1994). Each database relates multifrequency brightness temperatures (TBs) to microphysical profiles that describe the space–time properties of a precipitating system. Smith et al. (1994b), Smith et al. (1995), and Panegrossi et al. (1996) have described in more detail a series of cloud-model-derived databases. The microphysical profiles are made up of one or more categories of precipitating and suspended liquid and frozen hydrometeors (e.g., a four-component system might consist of cloud drops, rain drops, ice crystals, and graupel particles). The basic methodology for incorporating the profiles into the cloud–radiation database is to associate vectors of multifrequency TBs to each of the profile sets through a radiative transfer (RTE) model. These relationships, along with radiometer-measured TBs, are then used in some type of inversion procedure to retrieve actual liquid water content/ice water content profiles for the various hydrometeor categories.

To perform the inversion, two schemes may be used:

Corresponding author address: Dr. Giulia Panegrossi, Department of Atmospheric and Oceanic Sciences, University of Wisconsin—Madison, 1225 W. Dayton Street, Madison, WI 53706.
E-mail: giulia@meteor.wisc.edu

the first uses a transform operator to enrich the number of possible profiles in the database and then an estimator (Marzano et al. 1994; Mugnai et al. 1994; Evans et al. 1995; Pierdicca et al. 1996), while the second uses the cloud–radiation database as a source of initial guess information to seed an iterative solver that incorporates a forward RTE model and an optimization technique to perturb the initial guess profile toward a solution where the modeled TBs match the measured TBs (Kummerow and Giglio 1994a,b; Smith et al. 1994b).

From a purely physical perspective, there are three shortcomings in physical inversion profile schemes. The first is that they are vulnerable to the weaknesses and approximations of the cloud model, to the extent that the transform operator or iterative–optimization procedure cannot abstract the correct solution from a flawed set of microphysical profiles. Clearly, all limited-area, mesoscale, and cloud models contain a host of problems in replicating the physics and dynamics of the real atmosphere, not to mention problems with the microphysical parameterizations which are of direct concern to this study. Such weaknesses will not easily go away; however, all models generally improve with time, which will, in turn, lead to improved physical–inversion algorithms.

The second shortcoming stems from the RTE modeling. Generally one-dimensional (1D) RTE models are used that do not account for the true three-dimensional (3D) finite structure of clouds and precipitation. It has been shown, for example, that plane-parallel TBs are generally less (larger) than 3D TBs at the higher (lower) frequencies (Haferman et al. 1994; Roberti et al. 1994), and that 1D TB signatures, expecially at lower frequencies, exhibit geometric displacements when compared with those of 3D models (Roberti et al. 1994). In this study we focus on the impact of cloud model microphysics on precipitation retrieval based on plane-parallel RTE modeling. The analysis of 3D effects is beyond the scope of this paper and would require a separate study to fully understand their effects on retrieval. Moreover, all hydrometeor components are usually approximated as spherical scatterers because such an approximation favors single scatter computational efficiency and avoids some perplexing problems that arise when trying to assimilate nonsphericity into the multiple scattering model. By the same token, such simplifications, as well as any further simplifications used in either the single or multiple scatter calculations, generally misrepresent the true TB–rain rate relationships.

The third shortcoming is that physically based algorithms using a forward RTE model are computationally intensive if an iterative approach is used because numerous radiative transfer calculations are required (Smith et al. 1994a). As processor speeds on workstations increase, concerns with this issue are diminishing and to some extent such a computational problem can be mitigated with massive look-up table techniques. This problem is less of an issue in the transform approach where the time-consuming task of solving the radiative transfer equation is accomplished only once, when generating the enriched cloud–radiation database.

This paper explores a facet of the first two problems, involving partial mismatch of the cloud–radiation databases and the passive microwave measurements to which the retrieval algorithm is applied. By mismatch we mean that the N-dimensional TB domain (i.e., N frequencies) of a cloud–radiation database does not completely overlap the N-dimensional TB domain of the measurements themselves. We refer to these domains as the model manifold and the measurement manifold of TB space, respectively. Obviously, if the model manifold does not coincide with or is not a superset of the measurement manifold, then there are potential problems in associating rain rates to measurements whose TB vectors lie outside the model manifold, particularly if they are far removed. In practice, this happens if the model manifold's boundaries (in a Euclidean sense) fully or partially underlap those of the measurement manifold, and/or if the model manifold contains holes, gaps, or uneven sampling that are not consistent with the distribution of the measurement manifold.

A number of factors in the modeling can prevent total overlap of the measurement manifold by the model manifold. As noted, the 3D geometry can be a source of inconsistency. Imperfectly specified microphysical factors associated with hydrometeor size distributions, shape, and dielectric properties are sources of mismatch. Notwithstanding the potential influence of the latter two factors on the model manifold, we focus here on the size distribution factor, which is the more important of the three. There are also macrophysical factors associated with the properties of the hydrometeors, such as the relative mix of suspended and precipitating hydrometeors of either the liquid or frozen kind, and their vertical distributions. In the modeling, we allow for five or six constituent hydrometeor categories: 1) cloud drops, 2) rain drops, 3) graupel and hail, 4) pristine ice crystals, 5) snow flakes, and 6) aggregates of crystals and snow flakes. With such combinations it becomes essential to understand how mixing of the hydrometeors and their vertical distributions influence the model manifold. In a series of theoretical studies Mugnai and Smith (1988), Smith and Mugnai (1988), Mugnai et al. (1990, 1993), and Smith et al. (1992) examined how microphysical properties of convective systems determine the behavior of multispectral upwelling TBs. These studies have been very helpful in understanding how the vertical distribution and the mixing of liquid and frozen hydrometeors produce distinct TB signatures directly and indirectly associated with rainfall.

As part of the macroscale issue, there are two additional issues of interest: The first pertains to the spatial resolution over which the microphysics are allowed to vary, while the second pertains to the degree of inhomogeneity allowed for within the highest resolved scale. How these issues are handled in the modeling impacts

the model manifolds, as well as affects the interpretation of the measurement manifolds.

Last, there are various environmental factors affecting the radiative transfer calculations, such as the assumed temperature and moisture profiles, and the temperature and the emissivity properties of the underlying surface. All these factors have their distinct influence on the model manifold.

The objective of this study is to explain how these microphysical, macrophysical, and environmental factors affect the model manifolds, and at the same time to find means to overcome manifold mismatches arising from the cloud–radiation database generation for a given precipitation climatology and a given passive microwave instrument. However, we will point out that eliminating the mismatch between a model and measurement manifold does not imply necessarily that a cloud–radiation database is appropriate for the retrieval of an observed precipitation system. Different cloud-model simulations can produce TB domains that overlap the TB measurement domain, while the retrieved profile estimates and associated surface rain rates, which strongly depend on the simulated cloud profile structures, can be intrinsically biased. Thus, it is important that appropriate cloud model simulations are matched to the different types of precipitation systems.

Section 2 describes the main thermodynamic and microphysical features of the three cloud model simulations used in this study to represent the model manifolds: a severe summertime continental thunderstorm in a subtropical environment, a severe summertime continental thunderstorm in a midlatitude environment, and an over-ocean depression–tropical storm–hurricane progression in the Caribbean basin. In section 3 we describe the methodology utilized to generate the cloud–radiation databases from the simulated microphysical profiles, as well as describing the Special Sensor Microwave/Imager (SSM/I) dataset used to build the measurement database. We then discuss the approaches used to evaluate the sensitivity of the model manifolds to the environmental factors and to the hydrometeor size distributions, and describe the retrieval algorithm used in the study. In section 4 we examine the main features of the cloud–radiation databases and the impact of the different thermodynamic and microphysical factors associated with the three simulations on the upwelling TBs. Section 5 examines the results of the sensitivity studies. Example comparisons between improved and original model manifolds are given, as well as comparisons between improved model manifolds and measurement manifolds. In section 6 we focus on the retrieval results to understand how the above-mentioned microphysical, macrophysical, and environmental factors affect the SSM/I retrieval of two individual storm systems selected for the second phase of the NASA WetNet Precipitation Intercomparison Project (PIP-2). This project has examined the performance of a large set of SSM/I precipitation retrieval algorithms (Smith et al. 1998). Final discussion and conclusions are offered in section 7.

2. Cloud model simulations

In this study, we use model-generated cloud–radiation databases obtained from the simulation results of two different 3D, nonhydrostatic mesoscale cloud models that incorporate explicit microphysical processes involving liquid and frozen hydrometeors. Three simulations have been considered that represent 1) an intense Caribbean hurricane evolving from the depression stage (HURRICANE), 2) a severe continental thunderstorm in a subtropical summertime environment (COHMEX), and 3) a severe continental hailstorm in a midlatitude summertime environment (CCOPE). The first two simulations were produced by the University of Wisconsin Nonhydrostatic Modeling System (UW-NMS) (Tripoli 1992a). The third was based on the Hail Parameterization Model (HPM) version of the Wisconsin Dynamical/Microphysical Model (WISCDYMM) (Straka 1989; Johnson et al. 1993). The UW-NMS simulations are improved reruns of a previous COHMEX simulation used in Mugnai et al. (1990), Smith et al. (1992), and Mugnai et al. (1993), and of a Caribbean basin hurricane simulation [originally analyzed by Kanak (1990)], used in the algorithm developed at the Florida State University for purposes of the WetNet PIP-1 and PIP-2 retrieval calculations—see Smith et al. (1994b) and Wilheit et al. (1994). The improvements consist of using a better microphysical package, and for the HURRICANE simulation, of using a higher spatial resolution. The database drawn from the CCOPE simulation represents the first use of WISCDYMM microphysical output for passive microwave radiative transfer calculations.

Each simulation is used to generate a microphysical profile dataset, where each profile consists of five or six separate vertical profiles of the liquid and ice water contents (LWC and IWC) of the various hydrometeor types: cloud drops, rain drops, pristine crystals, ice crystal complexes (i.e., snow flakes and/or aggregates), and frozen graupel/hail particles. Then, a corresponding cloud–radiation database is generated by calculating the upwelling TBs from an RTE model for each individual microphysical profile.

The differences between these three cloud–radiation databases can be attributed not only to the different dynamical and microphysical features of the simulated storms, but also to the differences in the cloud models. For this reason, in the next two sections we will point out some of the main features of the cloud models, especially the microphysical parameterizations used for the various hydrometeors, and will describe the main thermodynamic and microphysical aspects of the simulated storms, which can be useful in the interpretation of the simulated TBs.

a. Cloud model hydrometeor parameterizations

Both WISCDYMM and UW-NMS are nonhydrostatic, 3D, and time-dependent cloud models that use bulk microphysical parameterizations and mass-weighted mean terminal velocities (Johnson et al. 1994; Tripoli 1992a). Mixed-phase particles (e.g., melting graupel) are not included, however, any combination of liquid and frozen particles is allowed to occur at any grid point. The dynamical equations and the microphysical processes leading to hydrometeor formation and evolution, as well as the parameterization of the hydrometeor categories, are treated differently in the two models.

The WISCDYMM (Johnson et al. 1993) uses five different hydrometeor types: 1) cloud droplets, 2) ice crystals, 3) snow crystals, 4) rain drops, and 5) graupel/hail particles. Equations and parameters of the microphysics are based on formulations given in Lin et al. (1983), and Cotton et al. (1982, 1986). There are a total of 38 microphysical processes incorporated in the model including nucleation, condensation, evaporation, freezing, melting, sublimation, deposition, autoconversion, and accretion (Straka 1989).

For rain, snow, and graupel/hail the HPM version of WISCDYMM utilizes a Marshall–Palmer distribution:

$$n(D) = A \exp(-BD), \tag{1}$$

where B and A are derived by the model at each grid point. The intercept (A) of rain size distribution is fixed at 8×10^6 m^{-4}. The median volume diameter of each hydrometeor is given by

$$D_c = 3.67/B. \tag{2}$$

For snow and hail/graupel, the densities are equal to 100 and 900 kg m^{-3}, respectively.

Ice crystals and cloud water drops are assumed to be monodispersed, and the model provides their mass and diameter at each grid point. The concentration of the cloud water drops is fixed at 7×10^8 m^{-3}. For ice crystals, the maximum number concentration is 1×10^9 m^{-3} at temperatures below 230.95 K, decreasing exponentially to 0 at T $>$ 273.16 K. Ice crystal density is fixed at 570 kg m^{-3}.

The UW-NMS (Tripoli 1992a) is a further development of the Regional Atmospheric Modeling System maintained at Colorado State University (CSU-RAMS) (see Tripoli and Cotton 1982, 1986, 1989; Cotton et al. 1982; 1986; Pielke et al. 1992). A two-way multiple-nested grid system is employed, allowing any nest to move along a specified trajectory or to move with the surface pressure minimum. The UW-NMS microphysical module is a modified form of the cloud microphysics module of CSU-RAMS (Flatau et al. 1989). It predicts, at any grid point, the mixing ratios of 1) total water, 2) rain drops, 3) graupel particles, 4) pristine crystals, 5) snow crystals, and 6) aggregates. Depending on the application, all or some of these categories may be selected. Each category may grow independently from vapor and self collection or may interact with the other categories through collision and coalescence. Temperature, potential temperature, pressure, water vapor mixing ratio, and cloud water mixing ratio are all diagnostically determined on the assumption of zero supersaturation with respect to water and the instantaneous growth and evaporation of cloud drops in response to changes in supersaturation. A detailed description of the formation and interaction processes between the various hydrometeor categories can be found in Tripoli (1992b).

For the present simulations, the constant-slope Marshall–Palmer size distribution parameterization assumed in the old version of the COHMEX simulation (Smith et al. 1992) is maintained for rain, graupel, and aggregates. However, treatment of the other categories has been changed. The cloud category is treated with a constant size distribution and the original pristine crystal category is divided into a snow category and a pristine crystal category.

For clouds, we found a characteristic radius of about 1×10^{-2} mm from the simulations. The modified pristine category is assumed to be composed of newly nucleated hexagonal plate crystals of uniform mass that melt instantaneously when the temperature of the air exceeds freezing. The uniform mass is assumed to be 1.5×10^{-9} kg, the density 220 kg m^{-3}, and the mean radius, calculated according to Flatau et al. (1989), is 1.17×10^{-1} mm. The new snow category follows a Marshall–Palmer size distribution with slope and intercept derived from an explicitly predicted number concentration per unit mass. Snow crystals, as well as aggregates, have a size-dependent density $\rho_{s/a}$ given by

$$\rho_{s/a} = \frac{15}{(2r)^{0.6}} \text{ [kg m}^{-3}\text{]}, \tag{3}$$

where r has to be specified (in centimeters).

Table 1 summarizes the particle density and size distribution parameterizations in the three simulations. The values of the characteristic radii not specified in the models have been obtained from a statistical analysis of the simulation outputs. In the CCOPE simulation, the characteristic radii of rain, graupel, and snow have been obtained with Eq. (2) and from the values of the slope of the Marshall–Palmer size distribution given at each grid point. In the HURRICANE simulation, aggregated crystals are assumed to be part of the snow category and the characteristic snow radius is limited to 1.65 mm. In the COHMEX simulation, the aggregate category is treated separately from snow; the characteristic radius is 1.65 mm for the aggregates and 5×10^{-1} mm for the snow. Except for the different treatment of snow and aggregates, the COHMEX and HURRICANE simulations use the same microphysical parameterization. In contrast, the large differences of the ice phase categories are evident in the CCOPE simulation with respect to the COHMEX and HURRICANE simulations. First, the CCOPE monodispersed ice particles have sizes

TABLE 1. Size distribution parameters and particle densities: M–P indicates the Marshall–Palmer size distribution; (*) indicates the values of characteristic radii not specified in the models that have been obtained from a statistical analysis of the simulation outputs; (**) indicates the particle densities calculated according to Eq. (3). The reference values given are obtained for $r = r_c$.

	r_c (mm)	Size distribution function	ρ_c (kg m^{-3})
		COHMEX	
Cloud	1×10^{-2}(*)	monodispersed	1×10^3
Rain	2.7×10^{-1}	M–P	1×10^3
Graupel	5×10^{-1}	M–P	6×10^2
Pristine ice	1.17×10^{-1}	monodispersed	2.2×10^2
Snow	5×10^{-1}	M–P	6×10^1(**)
Aggregates	1.65	M–P	3×10^1(**)
		HURRICANE	
Cloud	1×10^{-2}(*)	monodispersed	1×10^3
Rain	2.7×10^{-1}	M–P	1×10^3
Graupel	5×10^{-1}	M–P	6×10^2
Pristine ice	1.17×10^{-1}	monodispersed	2.2×10^2
Snow/aggregates	1.65	M–P	3×10^1(**)
		CCOPE	
Cloud	$(0.1–1) \times 10^{-2}$(*)	monodispersed	1×10^3
Rain	$5 \times 10^{-2} - 3$(*)	M–P	1×10^3
Graupel/hail	0.2–5.5(*)	M–P	9×10^2
Snow	$1.38 \times 10^{-1} - 4$(*)	M–P	1×10^2
Ice	$1 \times 10^{-2} - 5$(*)	monodispersed	5.7×10^2

ranging over a wide interval with a density that is ~2.5 times that assumed for pristine crystals in the UW-NMS. Second, the CCOPE hail/graupel particles have larger sizes (as confirmed by the hail observations during the storm) with much larger density. Finally, the constant value assumed for the snow density in the CCOPE simulation is relatively large. According to Eq. (3), which gives the density–diameter relationship for snow crystals and aggregates in the UW-NMS, the snow density assumed in the CCOPE simulation corresponds to particles of a diameter $\sim 4 \times 10^{-1}$ mm. Thus, the density of snow crystals with diameters larger (smaller) than 4×10^{-1} mm is overestimated (underestimated).

b. Highlights of storm simulations

The WISCDYMM has been used by Johnson et al. (1994) to simulate and examine, in detail, the microphysical features of a highly glaciated and intense supercell storm that passed through the Cooperative Convective Precipitation Experiment (CCOPE) observation network in southeastern Montana on 2 August 1981. The simulation was performed over a period of 2.5 h using a horizontal grid spacing of 1 km over a 55×55 km^2 domain, and a vertical resolution of 500 m over a 19-km depth. This grid spacing was found to resolve adequately the dynamics of the storm, as there are 8–12 grid points across the main axis of the precipitation cloud. The sounding used in the initialization was from Knowlton, Montana, which was located in the storm inflow 90 km east-southeast of the storm. The CCOPE storm simulation exhibits dynamic and thermodynamic features characteristic of the actual storm, including an intense and persistent updraft in excess of 55 m s^{-1}. Observations of the actual storm showed that copious amounts of hail were produced in the cloud and at the surface, with diameters as large as 88 mm. The simulation shows that more than 80% of the storm hydrometeor mass is ice, with graupel/hail being the most predominant type. The total mass of ice, snow, and graupel/hail increases rapidly with storm intensity, while the total liquid water mass consisting of cloud and rainwater increases much more slowly. The low rain content and the predominant presence of hail/graupel in the main core are the main features of the storm.

The UW-NMS has been used to simulate two events: 1) a meso-β-scale convective system near the Eldridge observation network, Alabama, on 11 July 1986 that occurred during the Cooperative Huntsville Meteorological Experiment (COHMEX); and 2) a tropical cyclone with an explicit representation of cumulus on a meso-β-scale grid and, for the last 6 h, on a meso-γ-scale grid.

The COHMEX simulation was carried out for 4 hours on a square domain of 50×50 km^2 with 1-km grid spacing in the horizontal, and 42 levels in the vertical with spacing increasing from ~400 m below 2 km and expanding progressively to ~800–900 m above. Horizontally homogeneous initial conditions were composited from the upper-air sounding taken from Rainsville, Alabama, and from Double Springs, Alabama, on the time and location of this storm system. Examination of the storm evolution shows unusually long-lived cumulonimbus cells, although not supercells. An incipient first storm cell develops within the first half hour, later followed by the formation of a well-organized gust from east of the initial cell, along which new cells form and merge. By the second hour, the storm transforms to a

multicell storm system that continues to support a major central storm core and a large outflow boundary propagating toward the south. During this intermediate stage, a cirrus anvil develops and begins spreading to the northwest of the storm, with overhanging older cells left behind as the storm propagated to the east. Until 3 h 45 min of simulation time the initial cells, which slowly drifted to the west away from the main core region, change from strong convective towers to a wider-spread midlevel rain-producing system. The main core of the storm exhibits supercell characteristics. By the end of the fourth hour, the system reaches numerical steady state.

The tropical cyclone simulation was carried out for 56 h. It was initiated by a horizontally homogeneous basic thermodynamic structure taken from the temperature and humidity profiles observed at Kingston, Jamaica, 36 h before the passage of Hurricane Gilbert (9–16 September 1988). Initial mean winds were assumed to be zero. Four nested grids were used for the simulation. The grid locations, spacing, and lengths are described in Tripoli (1992b), together with time steps, implementation period, and the initial perturbation details. The outer grid was centered along the expected path of the modeled storm, the medium grid was centered over the location of the initial perturbation, the third grid was implemented after 8 h of integration when the cyclone stage begins, and the fourth grid with a 3.3-km horizontal resolution over a 205 $\times$ 205 km^2 domain, was implemented for the last 6-h period at the mature stage. The vertical grid spacing is the same of that used for the COHMEX simulation. In this study, we use the results from the inner grid. At this stage of the evolution, convection is limited to the eyewall and inner bands. The eyewall diameter is 120 km and the eye is about 30 km wide. The eyewall is constructed of several asymmetric bands of vertical motion. The cloud field seems to almost totally lack cumulus structure and gives the appearance of spiral shaped stratiform-like cloud. The eyewall and the rain bands are very well resolved.

Figure 1 shows the variability of the vertical profiles of temperature, water vapor mixing ratio, and vertical wind velocity for the CCOPE, COHMEX, and HURRICANE storm simulations. For each parameter, the percent distribution of the values at each vertical level is given in a grayscale. The mean temperature, water vapor, and vertical wind profiles of the three simulations reveal different thermodynamic and kinematics conditions for the storms. In particular, the water vapor mixing ratio profiles show that the CCOPE storm is much drier ($\sim$12 g kg^{-1} at the surface) than the UW-NMS simulations ($\sim$18 g kg^{-1} for the COHMEX and $\sim$22 g kg^{-1} for the HURRICANE). Furthermore, the CCOPE simulation shows a lower tropopause ($\sim$12 km) and a very different temperature profile than the COHMEX and HURRICANE simulation. As a consequence, the freezing level is $\sim$5 km in the CCOPE case and $\sim$9 and $\sim$8 km, respectively, in the COHMEX and HURRICANE cases. Finally, the very high values of the vertical wind velocity in the CCOPE storm simulation reveal its classic supercell features.

3. Methodology

a. Generation of cloud-radiation databases

Model variables acquired, at each horizontal grid point, are the vertical profiles of atmospheric temperature (T), atmospheric pressure (P), water vapor mixing ratio (q), vertical wind speed (w), and equivalent water contents (EWCs) of the various hydrometeors. The WISCDYMM also provides size distribution parameters of the hydrometeors. Before generating the cloud–radiation database, a thorough analysis of the storms at different stages of their evolution has been carried out in order to select representative storm features and time steps. In this process, we consider not only the microphysical structure of the storms, but also their top-down microwave appearance at the SSM/I frequencies, simulated by using the vertical profiles at each time step as input to the RTE model.

For example, the output of the COHMEX storm has been sampled every 15 minutes (for a total of 16 time steps) throughout the simulation, providing 2500 data points each minute (50 $\times$ 50 pixels at 1-km resolution). For the CCOPE simulation, we have selected 16 time steps (every 10 min), each with 3025 data points (55 $\times$ 55 pixels at 1-km resolution). During the mature stage of the HURRICANE simulation, six representative time steps from the 49 available have been selected, each with 3844 data points in the 205 $\times$ 205 km inner nest region of the storm (62 $\times$ 62 pixels at 3.3-km resolution).

In order to generate cloud–radiation databases consistent with the horizontal resolution of the measuring radiometer, we have considered horizontally homogeneous cloud boxes having a horizontal dimension of $\sim$10 $\times$ 10 km^2, comparable to the ground footprint dimensions of the highest SSM/I frequency, that is, 85 GHz. For each selected time step of each simulation, we calculate the horizontally averaged profiles of the various hydrometeors and environmental parameters for all cloud boxes, obtained by moving the box volume within the horizontal storm target stepwise across all grid points. We refer to each set of vertical profiles as a database realization, or a data point. In the COHMEX and CCOPE simulations, the averaging is performed on boxes having a horizontal dimension of 10 $\times$ 10 km^2 (10 $\times$ 10 data points), whereas, for the HURRICANE, the averaging is performed on boxes of 13.2 $\times$ 13.2 km^2 (4 $\times$ 4 data points). By taking running averages, we simulate the smoothing effect of the SSM/I measurements.

From an analysis of these data points, we determined that cloud structures with low hydrometeor mass contents cover most of the target domain and define a highly

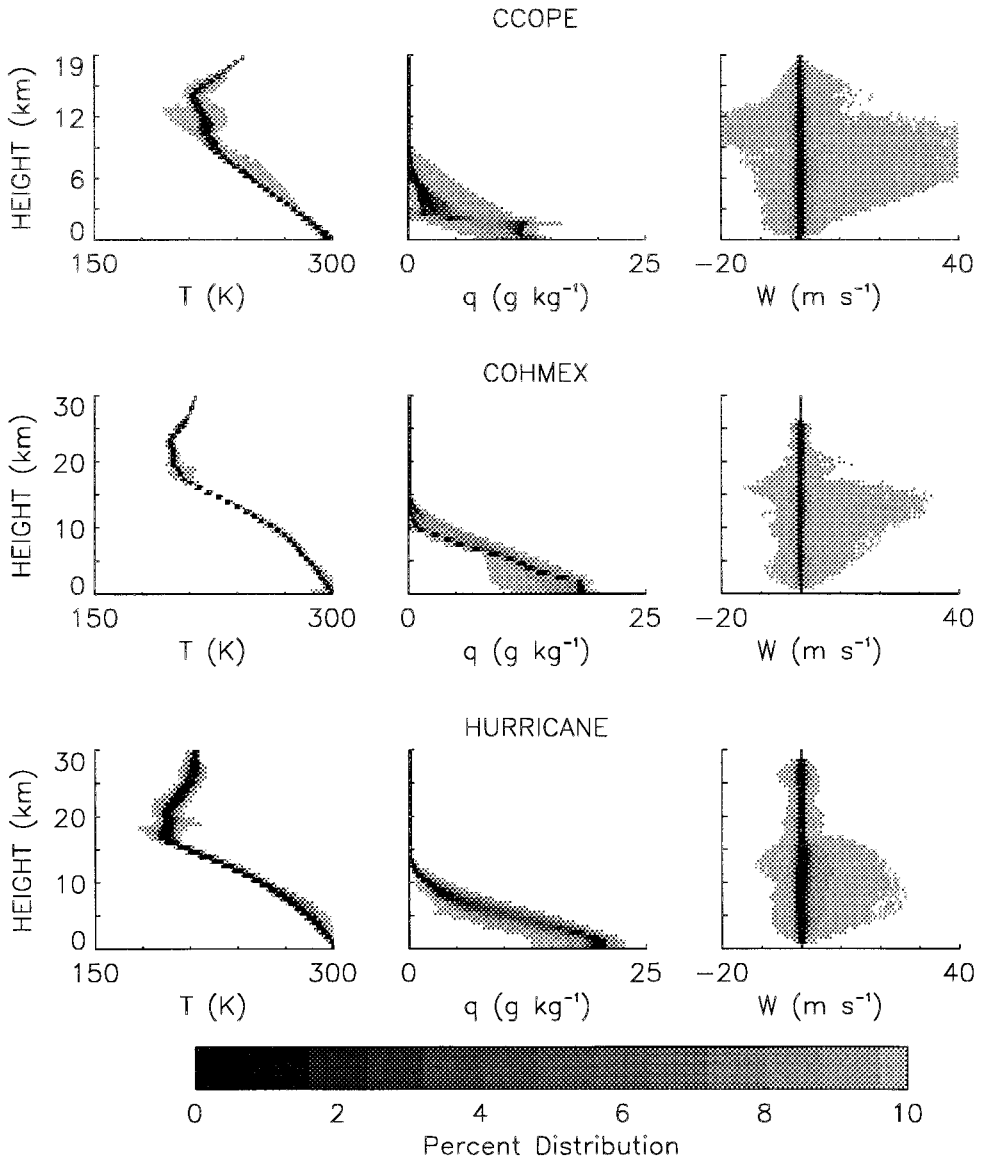

FIG. 1. High-resolution variability of the vertical profiles of temperature, water vapor mixing ratio, and vertical wind velocity for the CCOPE, COHMEX, and HURRICANE storm simulations. For each parameter, the percent distribution of the values at each vertical level is given by the grayscale.

dense portion of each database. Thus, it is possible to create a smaller and more manageable database by applying a selection procedure that eliminates the redundant weak cloud structures, while preserving the less dense portion of the database, which is characterized by more intense cloud structures generally associated with precipitation. As a result, totals of 14 702, 9273, and 17 701 low-resolution realizations have been obtained for the CCOPE, COHMEX, and HURRICANE databases, respectively.

In order to study the impact of horizontal resolution and inhomogeneity on the model manifolds, we generate corresponding high-resolution databases by considering the hydrometeor and environmental profiles at the original resolutions of the cloud models. After applying the aforementioned cloud-structure selection procedure, totals of 9471, 4276, and 20 081 high-resolution realizations have been obtained for the CCOPE, COHMEX, and HURRICANE databases, respectively.

The vertical profiles of the selected data points have been used as input to the RTE model. Calculations are made at the four SSM/I frequencies of 19.35, 22.235, 37.0, and 85.5 GHz, as well as 10.7 GHz, which is used on the airborne Advanced Microwave Precipitation Radiometer (AMPR) (Spencer et al. 1994) and will be used on the future Tropical Rainfall Measurement Mission (TRMM) Microwave Imager (TMI) (Simpson et al. 1996). For this study, we mostly focus on the SSM/I

TABLE 2. Surface emissivity assumed for land conditions at the four SSM/I frequencies.

Frequency (GHz)	19.35	22.235	37.0	85.5
Emissivity	0.81	0.82	0.84	0.85

window frequencies of 19, 37, and 85 GHz, considering unpolarized upwelling TBs obtained at an incident angle of 53.1°, consistent with the SSM/I instrument's conical scan viewing.

The RTE model is a polarized Sobolev two-stream solution of the azimuthally independent form of the radiative transfer equation (Smith et al. 1994b). It was developed from an azimuthally dependent model designed for solar spectrum applications described by Xiang et al. (1994). It is designed to simulate brightness temperature measurements from any combination of polarized or unpolarized passive microwave channels. The required inputs to the model are the temperature and moisture profiles, the temperature and emissivity of the surface, and the EWCs of the various hydrometeors. Absorption by gases at the microwave frequencies is modeled using a combined water vapor–oxygen volume absorption coefficient obtained from the clear-air refractivity model described by Liebe and Gimmestad (1978) and Liebe (1985). Mathematical details and results of a calibration study of the RTE model, helpful in understanding its contribution to algorithm uncertainty, are found in Smith et al. (1994b).

Surface emittance is a key parameter in microwave radiometry because the radiation emitted and reflected by the underlying surface may significantly contribute to the emerging radiances above a precipitating cloud, depending on the cloud's optical depth and the actual microwave frequency. In this study, both ocean and land have been assumed to be rough unpolarized Lambertian surfaces characterized by an average emittance ($\bar{\epsilon}$) independent of direction. In the ocean case, we have used the algorithm of Petty and Katsaros (1994) that generates wind-roughened horizontal and vertical emissivities of an ocean surface at SSM/I frequencies. Since the Frenel assumption is more often used to model the microwave radiative effects of the ocean surface, we have calculated the typical brightness temperature differences between Lambertian and Frenel assumptions for the ocean surface, and have verified that differences are not significant at the three SSM/I frequencies. Both at 19 and 37 GHz, the TBs calculated with the Lambertian assumption are generally slightly larger than those calculated with the Frenel assumption, while at 85 GHz the TBs are roughly the same. The largest difference at zero surface rain rate is $\Delta T \approx 3.5$ K and $\Delta T \approx 2.5$ K at 19 and 37 GHz respectively. The differences decrease as rain rate increases and are less than 0.5 K at rain rate larger than 20 mm h^{-1}, both at 19 and 37 GHz. The emittance of a land surface is highly variable and not well documented. In general, the magnitude of $\bar{\epsilon}$ decreases as soil moisture increases. However, for this study we have used invariant values as given in Table 2. For all calculations, temperature of the surface has been assumed equivalent to the atmospheric temperature immediately above the surface.

TABLE 3. Radius truncation limits assumed for Mie calculations.

	R min (mm)	R max (mm)
COHMEX		
Rain	1×10^{-1}	3
Graupel	1×10^{-1}	5
Snow	4×10^{-2}	1.65
Aggregates	1.17×10^{-1}	12.5
HURRICANE		
Rain	1×10^{-1}	3
Graupel	1×10^{-1}	5
Snow/aggregates	4×10^{-2}	12.5
CCOPE		
Rain	5×10^{-2}	3
Graupel/hail	2×10^{-1}	11
Snow/aggregates	1.38×10^{-1}	8

Since all particles are assumed to be spherical, scattering and absorption parameters can be calculated using Mie theory. The complex index of refraction of liquid and solid particles, as well as their relevant Mie scattering coefficients (absorption and scattering cross sections and asymmetry factors), have been calculated in the same manner described by Smith et al. (1992). Frozen particles are taken as a mixture of air and solid ice, so that their particle density is allowed to vary according to the type of hydrometeor being considered.

To reduce the computational requirements for the Mie calculations needed at all grid points in the cloud model space–time lattice, Mie coefficient look-up tables are generated, taking into account the different microphysical parameterizations of the hydrometeor categories in each simulation. For each hydrometeor category, the Mie coefficients are stored for the five microwave frequencies of interest, at 13 temperatures covering the range of atmospheric temperature variation, at preselected radii extending over the size range of the polydispersed hydrometeor categories. The size range limits of each hydrometeor category are summarized in Table 3. For the monodispersed cloud drops and pristine crystals of the COHMEX and HURRICANE simulations, Mie coefficients are stored for the mean radius of each category. The monodispersed ice crystals of the CCOPE simulation have mean radii that vary between 1×10^{-3} and 10 mm. For this reason we store Mie coefficients for some 200 radius categories so that at each model grid point appropriate coefficients can be selected according to the ice crystal diameter given by the model. The particle densities used in the Mie calculations are those given in Table 1.

Volume absorption and scattering coefficients and the asymmetry factor at a grid point are calculated by integrating the tabulated Mie coefficients over the appropriate size distribution. For the UW-NMS simulations,

the slope and intercept of the Marshall–Palmer size distribution of rain, graupel, snow, and aggregates have been derived according to Smith et al. (1992), while for the CCOPE simulation, we have assumed the values given by the model at each vertical level for each selected cloud structure.

b. Generation of measurement databases

The measurement manifold consists of SSM/I measurements taken from various cases selected for the second WetNet Precipitation Intercomparison Project (PIP-2); see Smith et al. (1998). The PIP-2 dataset is a set of 27 cases of various types of storm systems drawn from different years (1987–93), from different seasons during the year, over latitudes from 60°N to 10°S, and at a variety of different longitudes. Each case consists of one or more storm overpasses for a total sample of 118 targets, each of variable size ranging from 7×7 full-resolution pixels (90×90 km^2) to 64×128 pixels (830×1660 km^2). Here, full resolution is defined in terms of SSM/I A-scan pixels. The targets represent a mixture of land-only, ocean-only, and mixed land–ocean rainfall situations.

Three PIP-2 land cases have been selected that exhibit similar environmental conditions to the COHMEX and CCOPE simulations: 1) the Valtellina Flood (23 August 1987), an intense mountain storm that produced damaging flash flooding in an alpine area in the Lombardia region of northern Italy (46.1°N, 9.4°E), entailing the largest storm of a major cloud system enveloping a complex of convective storm cells along a cold front over southern France and the northwestern alpine region of Italy; 2) a midlatitude cyclone occurring between 12 and 27 August 1992 that deepened over the North Atlantic and progressed over the British Isles and western Europe (53°–56°N, 3°–15°W); and 3) a summertime East Coast thunderstorm outbreak that occurred on 1 July 1992 producing a squall line over the western Maryland–eastern Pennsylvania region (40.2°N, 76°W). For the ocean measurement manifold we have selected five cases with tropical environmental conditions: (1 and 2) two deep convective cluster situations in the tropical western Pacific near Kwajalein Island (9°N, 168°E) that occurred on 5 August and 31 August 1992; 3) a western Pacific typhoon (17°–24°N, 126°–131°E) occurring between 10 and 14 July 1992 and reaching supertyphoon strength, eventually striking Japan and Korea and causing widespread damage and loss of life; 4) Pacific typhoon Oliver (15.6°N, 153°E) occurring on 7 February 1993 within the inner flux array of the Tropical Ocean Global Atmosphere Coupled Ocean–Atmosphere Response Experiment (TOGA COARE); and 5) a deep convection case within the TOGA COARE inner flux array (3°S, 157°E) that occurred on 13 December 1992.

From all overpasses available for the selected cases (three for land; five for ocean), we have generated two separate measurement manifolds. In so doing, the raw SSM/I TBs at 19 and 37 GHz have been spatially enhanced to the 13-km ground resolution of the 85-GHz channels using the Backus–Gilbert deconvolution technique developed by Farrar and Smith (1992) and Farrar et al. (1994). The unpolarized TBs at each frequency used for the measurement manifold have been calculated by taking the average of the vertical and horizontal brightness temperature components. The PIP-2 ''common screen'' procedure described by Ferraro et al. (1998) was used as a front-end rain detector to avoid spurious retrievals over nonraining areas.

c. Sensitivity studies

Sensitivity studies were carried out to analyze and separate the contributions of the various microphysical, macrophysical, and environmental factors on the modeled upwelling TBs so as to better understand their impact on the consistency of the model–measurement manifolds. As a first step, we have considered the situation in which the COHMEX, HURRICANE, and CCOPE low-resolution databases have the same underlying surface conditions described in section 3a (i.e., land and ocean surface emissivity). As a second step, we imposed the same meteorological profiles to all database realizations for each of the three simulations. These are used as input in the RTE modeling, to separate the effects of different environmental conditions of the simulated storms on the TBs from those factors related to their different microphysical and macrophysical features. We have selected meteorological profiles for two of the PIP-2 cases to generate the measurement manifolds. For the land case, we used the Valtellina Flood event obtaining profiles from the European Centre for Medium-Range Weather Forecasting. For the ocean case, we used the Typhoon Oliver event, obtaining profiles by averaging 50 soundings acquired during the TOGA COARE field phase (1 November 1992–28 February 1993).

Finally, as a third step, we used a common size distribution parameterization for the three simulations, allowing the rain, graupel, snow, and aggregate components to exhibit variable Marshall–Palmer slope and intercept properties at each vertical level. We note that the constant slope assumption used in the UW-NMS has strong impact on the Mie calculations and thus on the upwelling TBs. For each hydrometeor category, it does not account for the variation of the relative concentration of the particles of different sizes and with different optical properties, for a given total mass of ice or liquid at each grid point.

The details of the procedure used to modify the size distributions is described in the appendix. Basically, for each ice phase hydrometeor category, we consider the dependence of the intercept on the atmospheric temperature (Straka 1989). For graupel particles below the freezing level, this relationship has been combined with the equation that relates the intercept to the precipitation rate at each level (Pruppacher and Klett 1988; Ludlam

1994). The same equation has been considered for rain drops. By assuming a power-law relationship between the particle fall speed and diameter (Straka 1989), we obtain a precipitation rate directly related to the particle slope. Then, by considering the relationship between EWC at each level with the size distribution parameters, we can derive both slope and intercept.

d. Retrieval algorithm

To understand the fidelity of the databases generated from the three simulations for carrying out precipitation retrieval using SSM/I measurements, and the importance of using different simulations for the various typologies of precipitation events (characterized by different environmental conditions and different micro/macrophysical factors), we use a straightforward retrieval algorithm based on the Euclidean distance between the measured and modeled three-frequency TBs (19, 37, and 85 GHz). Before applying the algorithm, the raw SSM/I TBs of the selected precipitation event, are ''common screened'' and deconvolved with the procedures described in section 3b. For each pixel, all cloud-model structures whose simulated three-frequency TBs have a Euclidean distance from a measurement less than a given threshold are taken as possible solutions for the retrieval. For each of these, the surface rain rate is derived from a rain fallout formula that takes into account the rainwater EWC at the lowest level, and the raindrop mass-weighted mean terminal velocity parameterization assumed in the cloud models (see the appendix). The retrieval consists of calculating the mean hydrometeor profiles of the cloud structures that satisfy the TB threshold, along with the mean surface rain rate and associated variances. The variances provide the uncertainty limits of the estimates. In general, the TB threshold should be assigned so as to take into account the inherent instrument noise and modeling errors. In this study, a small value has been used ($\sqrt{3}$K), because we wish to examine the variances in the retrieved quantities when cloud structures from different simulations produce nearly the same microwave signature.

4. Key features of original cloud–radiation databases

In this section we analyze the original low-resolution cloud–radiation databases, that is, the databases generated using the original meteorological profiles and size distribution parameterizations described in section 2. We investigate the intercorrelations between the liquid and ice hydrometeors, in particular the correlations between hydrometeors that can be directly sensed at microwave frequencies with the surface rain rates. We then analyze the relationships between the upwelling TBs and the various hydrometeors.

In previous studies, Mugnai et al. (1990) and Smith et al. (1992) provided fundamental insight into the microwave emission and scattering properties of cloud structures containing a mixture of liquid and frozen hydrometeors. In these studies, they analyzed the underlying relationships between liquid and ice microphysics and the microwave characteristics of an earlier simulation of the COHMEX storm. They showed that graupel is the hydrometeor category best correlated to the TBs and that the correlation of the TBs with the surface rain rate is driven by its internal physical correlation with the graupel particles because cold rain microphysics is dominating the precipitation process in the storm simulation. In this section, we will show that the intercorrelation properties between the various cloud constituents and upwelling TBs are highly linked to the nature of the simulated storm (cold or warm rain microphysics), to the macrophysical and environmental features (mixing and vertical distributions of the hydrometeors, inhomogeneity, and meteorological profiles), to the cloud-model resolution, and to the microphysical parameterizations (hydrometeor size distributions).

Figure 2 shows the correlation diagrams of columnar graupel and rain EWCs with surface rain rates for the CCOPE (top), COHMEX (middle), and HURRICANE (bottom) low-resolution databases. It is evident that the CCOPE hailstorm is characterized by small mass contents of rain and light rain rates and large mass contents of graupel. The very intense nature of the tropical cyclone simulation is reflected in the large values of graupel and rain mass contents, and heavy surface rain rates. The correlations between columnar rain and surface rain rate are considerably larger than between columnar graupel and surface rain rate. The large correlations of graupel with surface rain rates in the CCOPE and COHMEX simulations are due to the cold rain microphysics in the main convective cells of the storms. In the HURRICANE database, the correlation diagram between graupel and rain rate is weaker because a large part of the domain is characterized by stratiform structures and warm rain, and the strong convection producing cold rain is limited to the cumulus structures in the rain bands and in the eyewall. In addition, the HURRICANE simulation is characterized by strong horizontal motion, while the updraft in many parts of the storm is smaller than in the two thunderstorm simulations. The combination of these two factors produces strong vertical shear between the ice and rain layers. The smaller updraft in many parts of the cyclone domain also explains the lower correlation between columnar rain and surface rain rate with respect to the two continental storms.

An important factor contributing to the different degrees of correlation between the cloud profile constituents among the three databases, as well as the large mass contents found in the HURRICANE, are the different timescales of horizontal transports and microphysical processes associated with the spatial resolution of the simulations. We have seen that these interrelated processes produce different degrees of inhomogeneities in the cloud structures of the low-resolution databases.

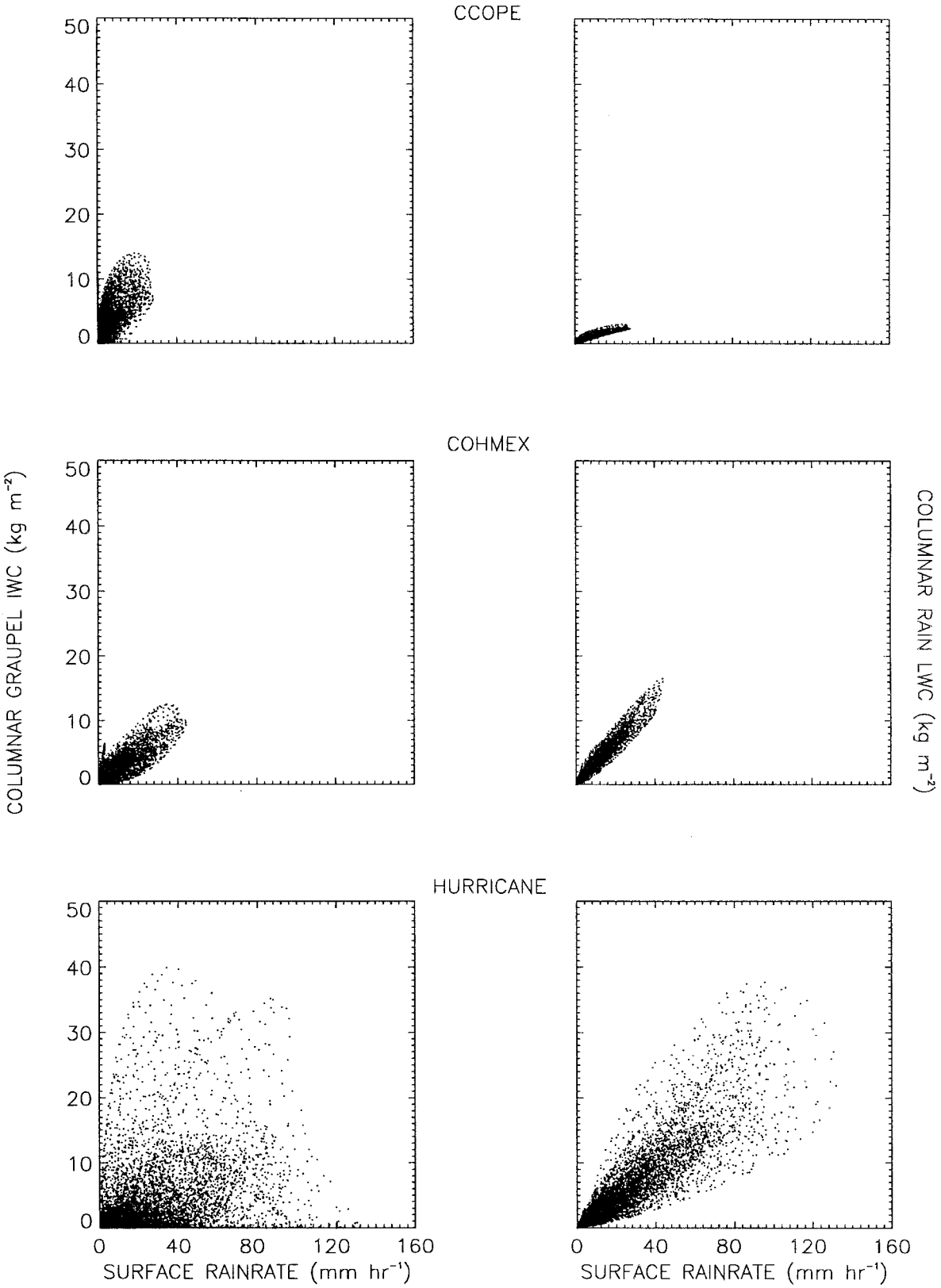

FIG. 2. Correlation diagrams between both columnar graupel and rain EWCs with surface rainrates for the CCOPE (top panels), COHMEX (middle panels), and HURRICANE (bottom panels) low-resolution databases.

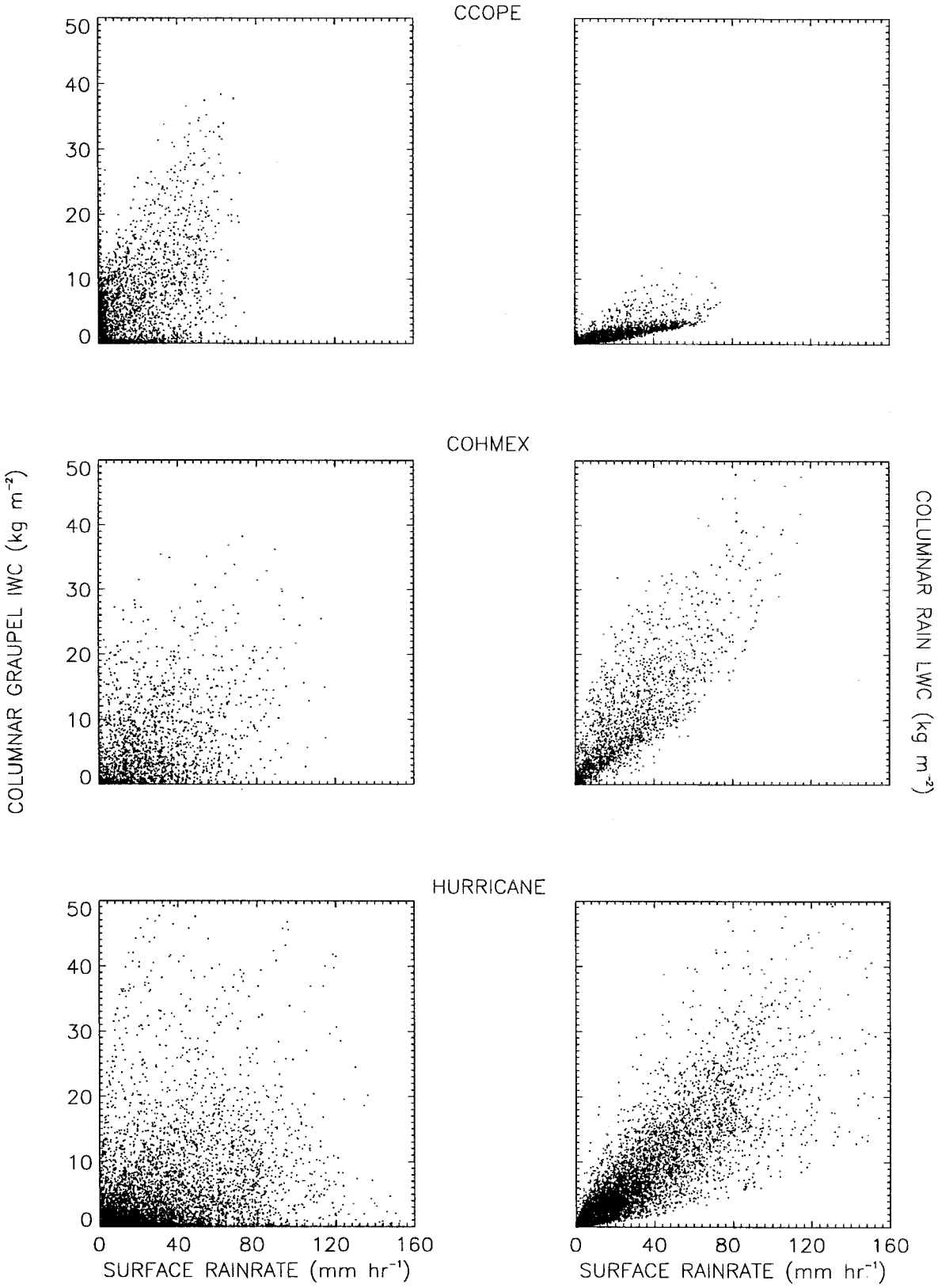

FIG. 3. Same as Fig. 2 except for the high-resolution databases.

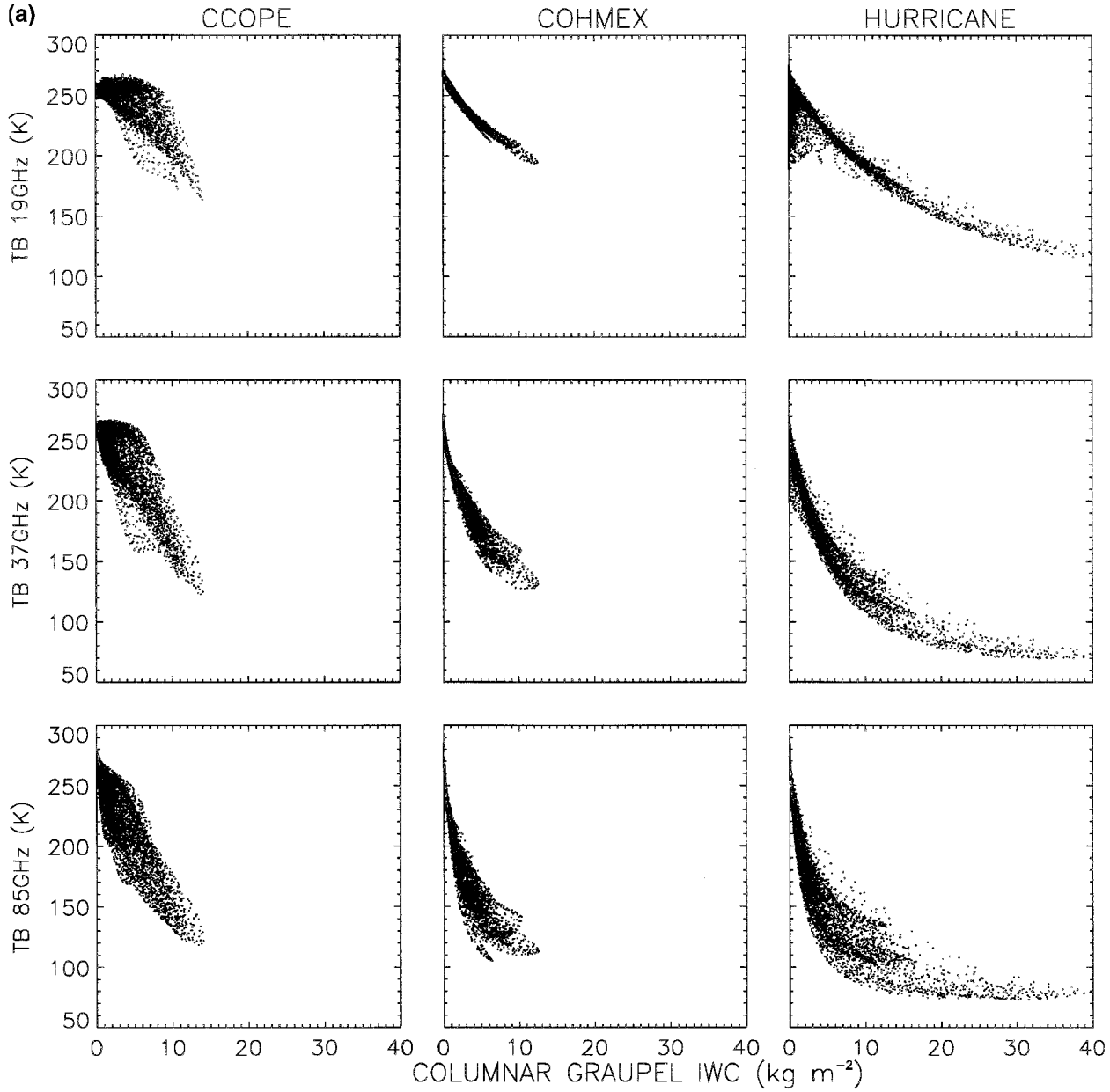

FIG. 4a. Correlation diagrams between TBs at 19, 37, and 85 GHz and columnar graupel EWC for CCOPE (left panels), COHMEX (middle panels), and HURRICANE (right panels) low-resolution databases.

Figure 3 shows examples of the correlation diagrams between columnar graupel and rain with the surface rain rate for the three databases generated at high resolution. Although all high-resolution diagrams exhibit larger values of columnar rain and graupel as well as surface rain rate, all the correlations are smaller. However, the changes are only significant for the CCOPE and COHMEX cases. The lower correlations arise because at high resolution, the effects of vertical shear on decoupling the ice and rain layers is enhanced. This demonstrates that horizontal averaging the cloud structures to the 10 $\times$ 10 km^2 gridscale filters out the effect of shear decoupling and improves the correlation between the icy upper layers and surface rain rates. This correlation shift is not nearly as evident with the HURRICANE case, partly because the highest resolvable features are approximately 10 times larger than in the CCOPE and COHMEX cases but also because the vertical coupling is not as strong. In such a large-scale system, it is likely that the upper-level anticyclonic outflow region decouples many of the generally smaller ice particles from the lower-level convective elements, thus diminishing ice–surface rain correlations.

The low-resolution databases contain less information

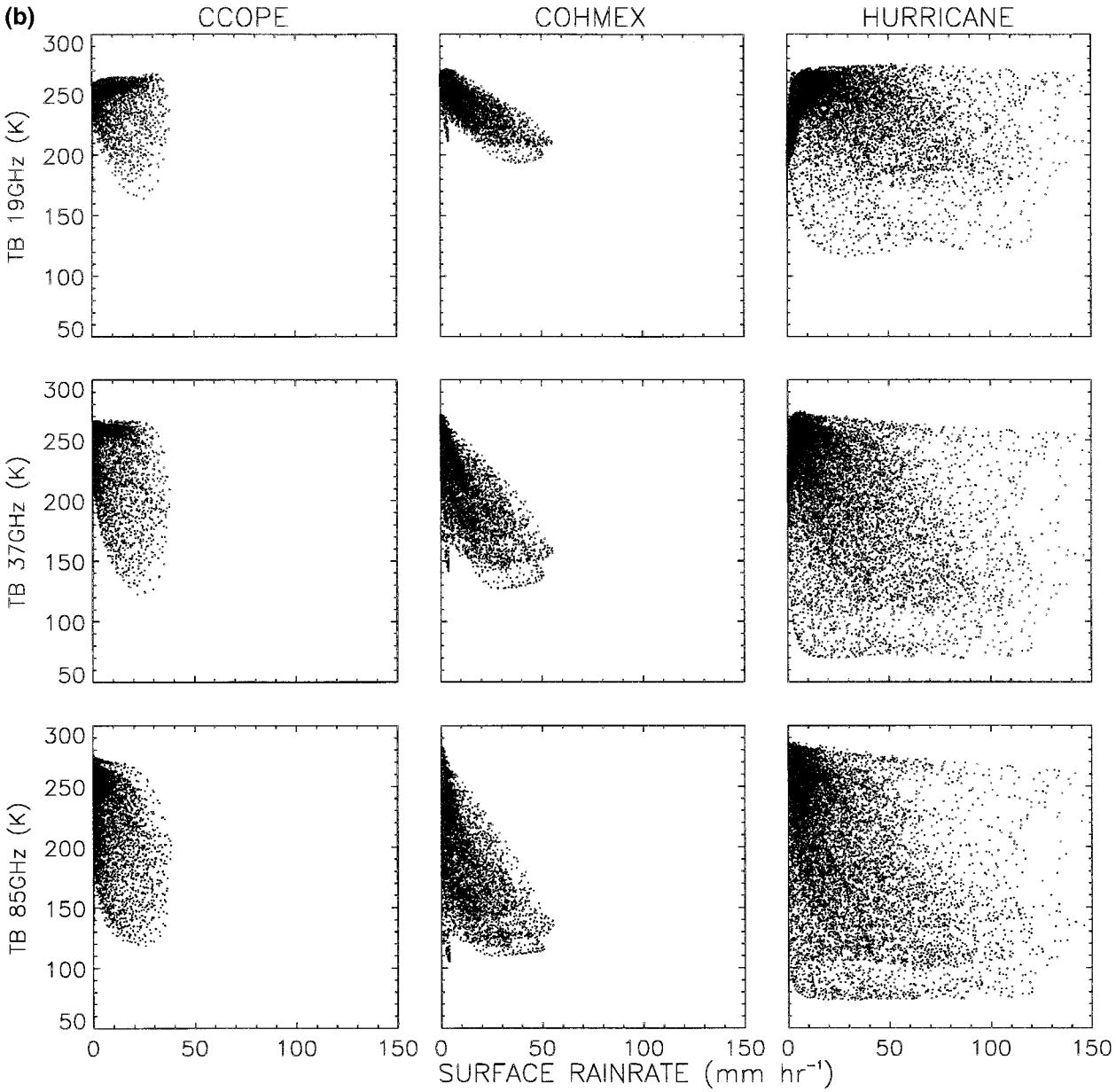

FIG. 4b. Same as (a) except for TB correlations with surface rain rate.

on the true nature of the simulated storms. For example, the correlation diagrams between graupel and surface rain rate in Fig. 3 reveal more clearly the different natures of the CCOPE and COHMEX thunderstorms, than do the corresponding diagrams in Fig. 2. In the CCOPE case, the correlation with graupel is larger than in COHMEX because the large vertical motions in the supercell produce entirely cold rain. In COHMEX, the cold rain is limited to the main convective cells, while the remainder of the domain is characterized by warm rain processes.

Figures 4a–b show the correlation diagrams of the TBs at 19, 37, and 85 GHz with both the graupel columnar EWCs and the surface rain rates for the three low-resolution databases. All but the HURRICANE case exhibit basic correlation between the TBs and surface rain rates, but the highest correlations occur between the TBs and graupel, even for the HURRICANE case. Earlier, Smith et al. (1992) made a detailed analysis of these same correlations, relating them to the emission and scattering properties of the hydrometeors and to their interactions within a precipitating cloud. Here we want to focus on the differences of these intercorrelations amongst various databases.

Part of the differences in the correlation relationships for the different storm cases arise from the different

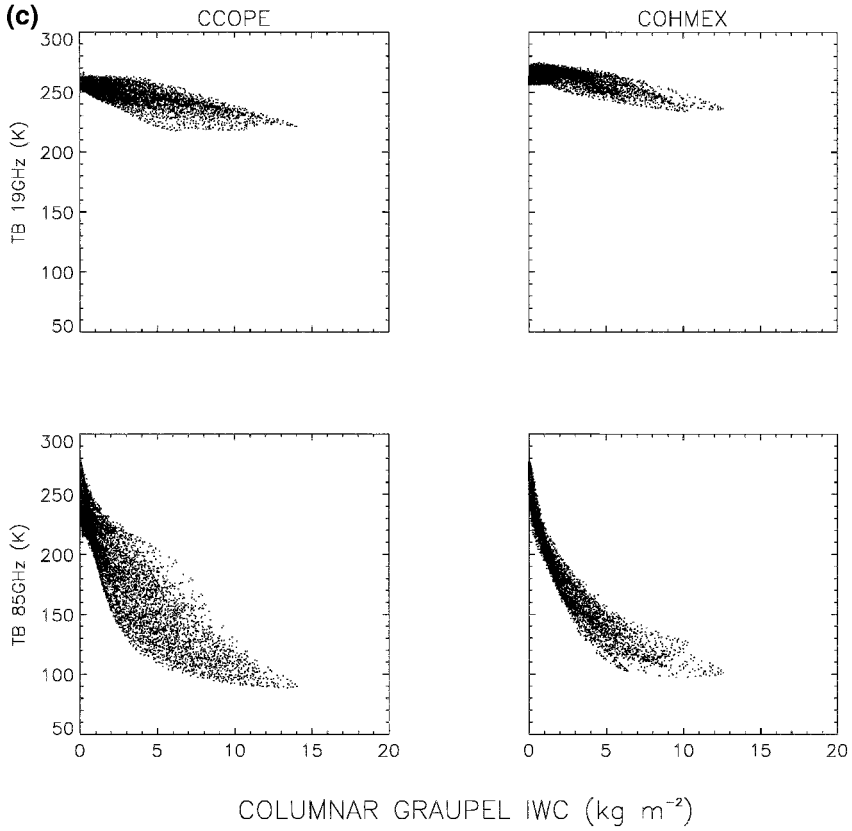

FIG. 4c. Correlation diagrams between TBs at 19 and 85 GHz and columnar graupel EWC for CCOPE (left panels), and COHMEX (right panels) low-resolution databases obtained with the modified size distributions.

surface emissivities used in the RTE calculations. This is most evident in the TB–graupel panels (Fig. 4a) when comparing the HURRICANE TB–ice relationships to the two sets of over-land relationships. The smaller surface emissivities for water lead to a distinct fold in the 19-GHz result and a smearing of the scatter diagram for small total graupel path lengths at 37 GHz. These same HURRICANE features are seen in the 19 and 37 GHz TB–surface rain rate diagrams, although the larger scatter in these relationships tends to obscure the fold pattern. The fold itself is simply a result of the contrast between the cold emitting surface and the warm emitting rain layers, which is more evident when the ice mass contents are small.

It is important to recognize that there are other major differences in the nature of the correlation relationships that stem from factors besides emissivity. For example, the more dominating role of cold rain microphysics produces the tighter TB–surface rain rate correlations for the CCOPE and COHMEX cases, relative to the HURRICANE case, whose warm rain features lead to large scatter.

Differences in the UW-NMS and WISCDYMM parameterizations for hydrometeor size distribution and ice density, particularly graupel, lead to the marked differences between the CCOPE and COHMEX TB–graupel relationships, as well as the TB–surface rain rate relationships. These same differences are apparent between the CCOPE and HURRICANE cases; however, the aforementioned emissivity and warm rain effects obscure these differences. Both the COHMEX and HURRICANE cases exhibit large TB correlations with the graupel that are mostly determined by the constant-slope Marshall–Palmer size distribution parameterization assumed in the UW-NMS. With this formulation, scattering increases only with mass content, not with the relative concentrations of large and small particles. For the CCOPE case, there is lower correlation between 19 GHz and graupel, related to the fact that the WISCDYMM allows for variable slope and intercept factors at each level of the cloud structures. To better understand the impact of the different size distributions of the models on the TB–graupel relationships, Fig. 4c shows the correlation of TBs at 19 and 85 GHz with graupel for the CCOPE and COHMEX databases obtained with the modified size distributions. With respect to the panels shown in Fig. 4a, a large increase of 19-GHz TBs is evident both for CCOPE and COHMEX, basically due to the smaller concentration of large particles in the modified parameterization. On the other hand, at 85 GHz

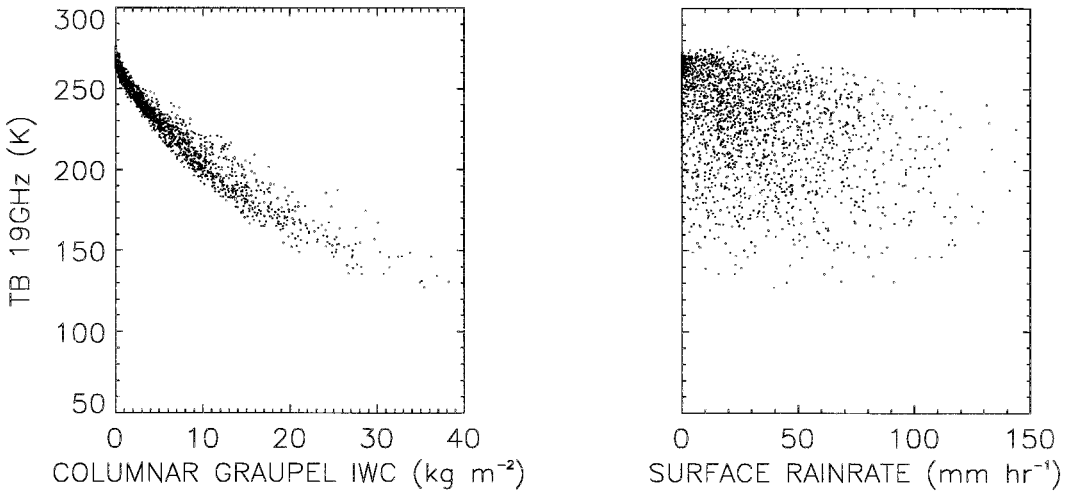

FIG. 5. Correlation diagrams between TB at 19 GHz and both columnar graupel EWC and surface rain rate for COHMEX high-resolution database.

the diagrams show a significant decrease of TBs only for CCOPE. The latter behavior can be explained by considering that the modified size distribution gives a higher concentration of small particles (due to the change of the intercept in the size distribution) with respect to the concentrations in the original CCOPE simulation. In the COHMEX simulation, the concentration changes are less significant and the resulting impact on the TBs negligible. It is worth noting that the TB–graupel correlation diagrams of both the CCOPE and COHMEX simulations at each frequency shown in Fig. 4c are much more similar to each other than those shown in Fig. 4a.

Further differences in the correlation relationships in Figs. 4a–b stem from differences in the environmental temperature–moisture profiles. The lower TB values for CCOPE, with respect to those of COHMEX and most evident for the smaller rain rates and graupel mass contents, are directly related to the lower temperatures below the freezing level and the lower boundary layer humidities. This effect is most evident at 19 GHz whose weighting function peak is closer to the surface.

Finally, the inherent horizontal resolution of the hydrometeor profiles strongly impacts the intercorrelation between the TBs and the rain–ice quantities. As an example, lower correlations are found for the high-resolution CCOPE and COHMEX databases. Figure 5 illustrates such correlations between 19-GHz TB and both columnar graupel and surface rain rate for the COHMEX high-resolution database. As discussed, the correlation falloff stems from the greater influence of vertical shear on the rain–ice decoupling at higher resolution.

The preceding analysis has demonstrated that the correlations between the TBs and the precipitation quantities, as well as the correlations between ice and rain, depend strongly on the intrinsic space and time scales of the simulated storm systems, microphysical details, and vertical environmental structures. This suggests that, in order to generate cloud–radiation databases appropriate for precipitation retrieval, close attention must not only be paid to the resolving power of the radiometer but also to the degree of inhomogeneity inherent to the storm simulation.

5. Comparison of measurement and model manifolds

In this section we analyze the results of the sensitivity studies described in section 3c, in order to differentiate the impacts of microphysical, macrophysical, and environmental factors on the model manifolds, and to overcome the mismatch between the measurement and model manifolds. Figures 6a,b show the measurement and model manifolds using color contour diagrams representing the projection of the boundaries of the three-dimensional brightness temperature vectors, in three two-dimensional TB planes, that is, 37–85 GHz (left panels), 19–85 GHz (middle panels), and 19–37 GHz (right panels). All axes range from 50 to 350 K. Each database is represented with a different color (red contours for COHMEX, green contours for HURRICANE, and blue contours for CCOPE). The black contours indicate the measurement manifolds. Over-land manifolds are shown in Fig. 6a, whereas over-ocean manifolds are shown in Fig. 6b. The first row of panels in each figure considers the model manifolds obtained with the original microphysical parameterizations and environmental profiles taken from the simulations. The second row of panels shows the results obtained by imposing the observational T–q profiles obtained from the Valtellina Flood and Typhoon Oliver events. The third row of panels shows databases generated using the observed environmental profiles and the modified size distribution parameterization.

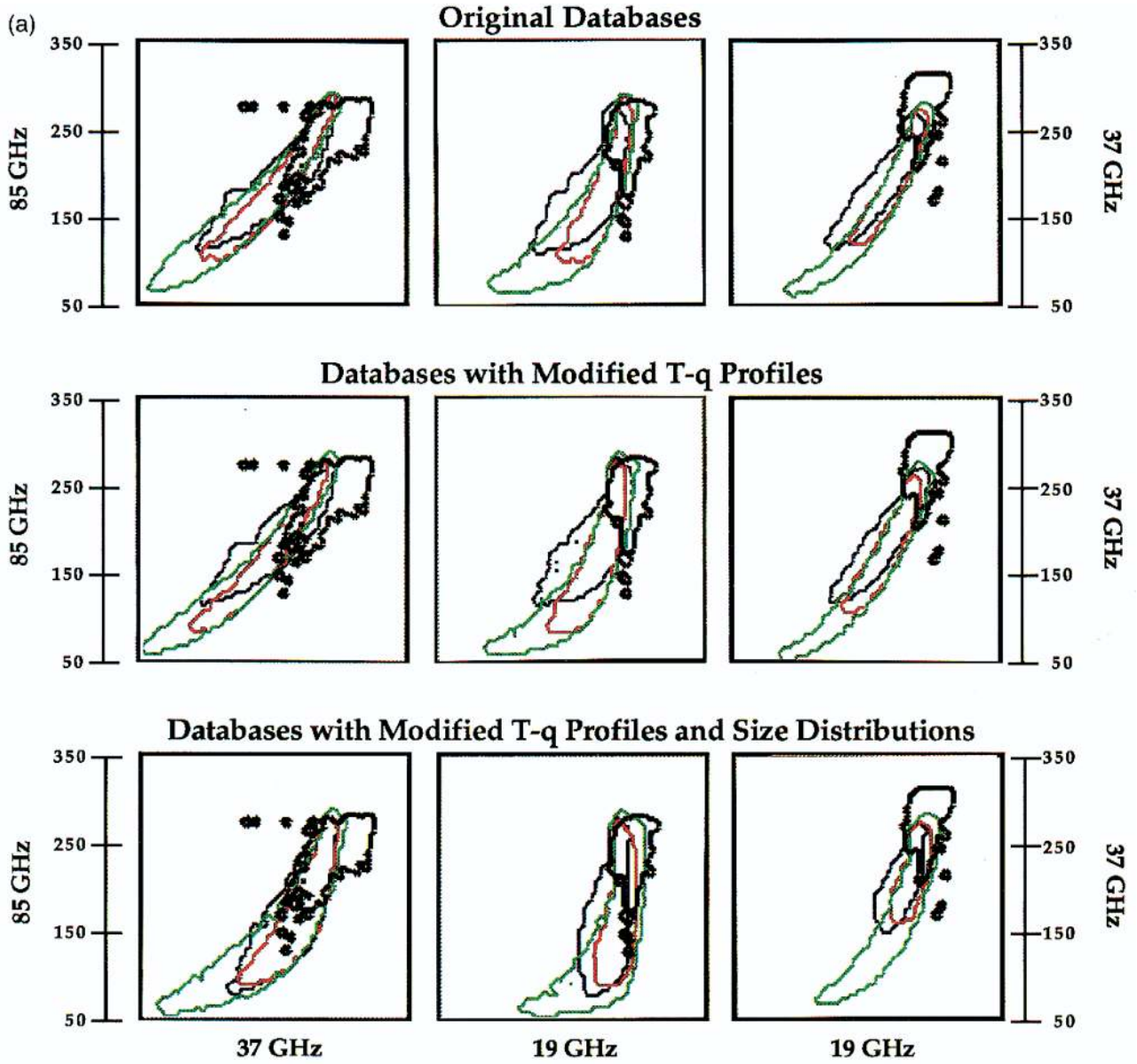

FIG. 6a. Color contour diagrams of over-land model and measurement manifolds. Each contour is the projection of the boundaries of the manifolds in the various two-dimensional TB planes: 37–85 GHz (left panels), 19–85 GHz (middle panels), and 19–37 GHz (right panels). Note the left ordinate labels (85 GHz) apply to both the left and middle panels, while the right ordinate labels (37 GHz) apply only to the right panels. The COHMEX boundaries are shown in red, the HURRICANE in green, and the CCOPE in blue. The measurement manifold boundaries are shown in black. The range limits of all axes are 50–350K.

a. Analysis of discrepancies with original model manifolds

From a qualitative analysis of the panels in the first row of both figures, it is evident that there are large differences in the contour shapes and the TB ranges occurring between the CCOPE and UW-NMS manifolds. Furthermore, there are significant mismatches between the measurement manifolds and all model manifolds for both land and ocean. By comparing each panel in the first row in Fig. 6a with the corresponding panel in Fig. 6b, it is possible to assess the effect of surface emissivity differences. All frequencies are influenced by surface emissivity, particularly when the cloud optical depths are small and contribute weakly to the upwelling radiation. However, as discussed in Mugnai et al. (1990), the influence of surface emission becomes negligible at high frequencies, even for light rain rates. All model manifolds contain lower temperatures than found with the measurement manifolds except for the over-land 85-GHz TBs of CCOPE. The bottom left portions of

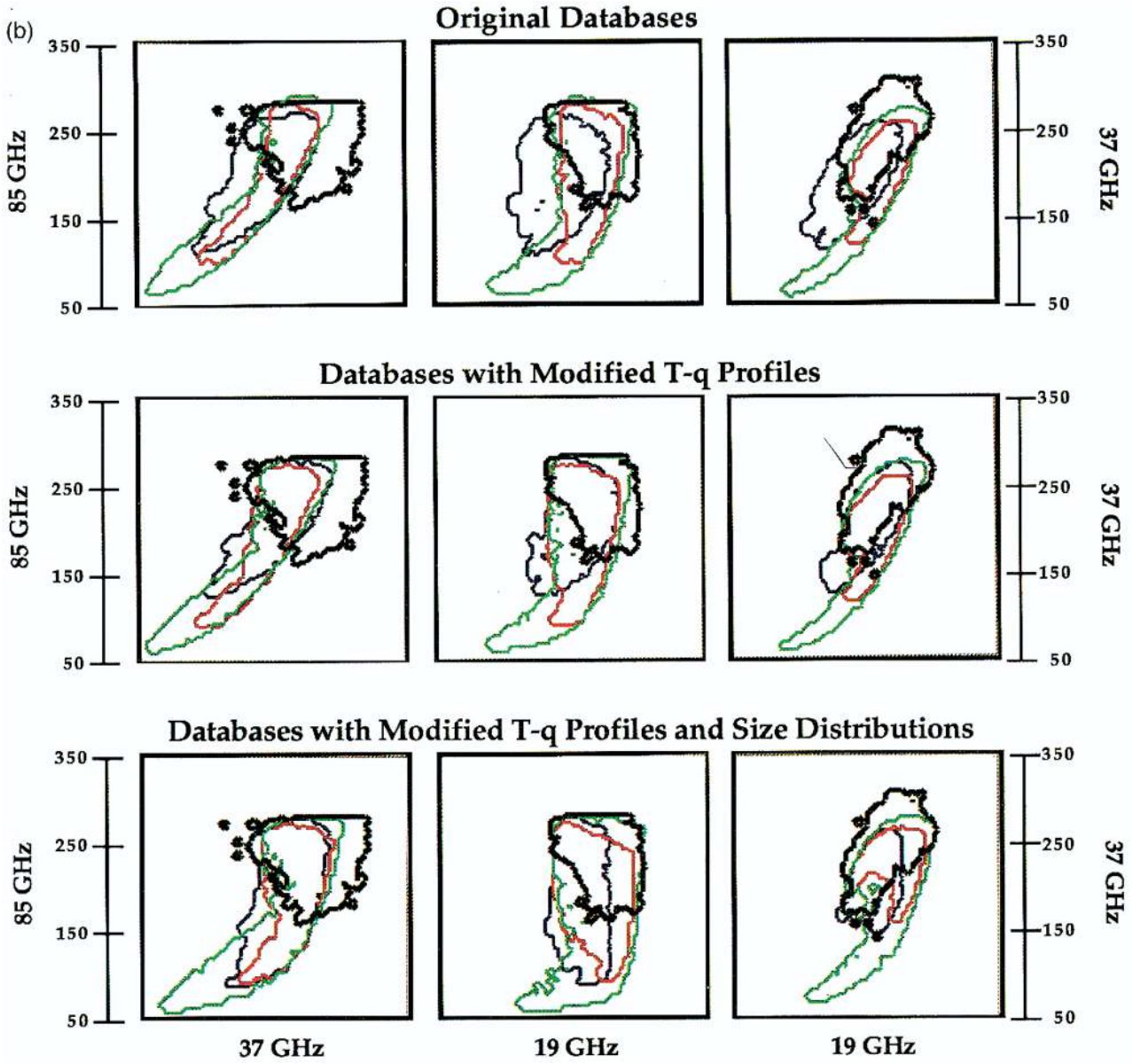

FIG. 6b. Same as (a) except for the over-ocean databases.

the contours over land, bounded by ~180 K at 85 GHz and ~200 K at 19 and 37 GHz in the COHMEX and HURRICANE databases, and by ~140 K at 85 GHz and ~200 K at 19 and 37 GHz in the CCOPE database, are similar in shape to the corresponding model tails over ocean. This is because these are the portions of the manifolds representing the most intense cloud structures where TBs are not affected by surface emissivity.

All over-land databases show strong correlation between the TBs at the three frequencies. This behavior is not matched by the measurements since the 19 and 37 GHz TBs never fall below 250 and 200 K, respectively, even when the scattering-depressed 85-GHz TBs fall to values around 130 K. An important factor that could contribute to this discrepancy is the difference in spatial resolutions between the measurements at 19 and 37 GHz and the modeled TBs calculated at 10-km resolution. The radiometer is not able to resolve the smaller intense ice core features of the storms that would decrease the TBs, not only at 85 GHz, but also at 19 and 37 GHz. The scattering effect that tends to shift the low TB part of the measurement manifold is smoothed at lower frequencies in which deconvolution does not completely eliminate the effect. For the ocean case, the model manifolds cover a generally wider volume in TB space than the measurement manifold. The contour

shapes of COHMEX and HURRICANE databases are similar and overlap with the measurements is close in the 19–85 GHz plane over ocean.

In the over-land CCOPE model manifold, the TBs at 19 and 37 GHz are shifted downward by 20–30 K, even in the upper right portions of the contours representing the less intense cloud structures where TBs are mostly affected by surface emissivity and environmental profiles. Over ocean, even greater shifts of 30–50 K are found with the 19 and 37 GHz TBs. This behavior at the lower frequencies is partly explained by differences in the environmental profiles, in particular the smaller water vapor mixing ratios and to the smaller temperatures below the freezing level of the CCOPE simulation. In addition, the CCOPE storm is characterized by low mass contents of rain in the lower layers (confined below the 5-km freezing level), leading to relatively weaker emission from the rain layers. The impact of these two factors on decreasing the TBs at the lower frequencies is greater over ocean because the TBs are more affected by the contrast between the radiometrically cold sea surface and the radiometrically warm rain layers.

It was noted in section 2a that the ice and graupel particle densities of the CCOPE storm are higher than those assumed in the COHMEX storm, while the mass contents of all ice phase particles are similar to COHMEX. For this reason we find smaller TBs at 19 and 37 GHz in the CCOPE model manifold (also smaller than either set of measurements). The higher correlation at the three frequencies in the COHMEX and HURRICANE manifolds with respect to the CCOPE manifold is attributed to the different size distribution parameterizations of the UW-NMS and WISCDYMM. The tilted elongated model manifolds of the COHMEX and HURRICANE simulations (more evident over ocean), representing strong correlation among all three frequencies, stems from the fact that the scattering due to ice particles is basically related to their mass contents. In the CCOPE simulation, the scattering by ice particles is related not only to their mass contents but also to their size distributions. The smaller TB values reached in the HURRICANE simulation are due to larger mass contents of large ice particles relative to CCOPE and COHMEX.

b. Sensitivity to meteorological profiles

In the second row in Figs. 6a–b, the model manifolds are created by using the observed environmental profiles from the Valtellina Flood and Typhoon Oliver events in the radiative transfer modeling. By imposing the same *T*–*q* profiles on the three simulation databases, we help quantify the impact of environmental conditions on the original mismatch between the model manifolds. Using common environmental profiles for the three simulations leads to a substantial improvement in the match-up between the model manifolds, particularly over ocean. However, at this stage, not much improvement is obtained between measurement and model manifolds. It is evident that the greatest changes are in the over-ocean CCOPE manifold. In the original simulation, the modeled *T*–*q* profiles differ significantly from those of a deep-ocean typhoon environment. The ocean profiles are characterized by a higher tropopause and larger temperatures and mixing ratios at the lower levels. In the RTE modeling, the larger thermometric temperatures of the rain layers plus the additional water vapor in and above the rain layers causes increased emission. As a consequence, all contours in the three TB planes are shifted to larger values, up to 30–40 K for the CCOPE manifold. In the COHMEX manifold, the TB contours are shifted downward by around 10 K at all frequencies. The HURRICANE TB space is not significantly affected by the modified environmental profiles (the shifts are more on the order of 5–10 K). This is because the *T*–*q* profiles of the HURRICANE simulation are very similar to those of the TOGA COARE environment.

Over land the changes in the modified model manifolds are less evident because the higher surface emissivities reduce the environmental effects on the upwelling TBs. Some changes in the TBs can be noted in the upper portion of the diagrams, where the cloud optical depths are small. The environmental conditions of the Valtellina event are similar to those of the CCOPE model environment, thus the modified TBs at all three frequencies undergo little change. In the HURRICANE and COHMEX model manifolds, TBs decrease by about 5–10 K with respect to the original manifolds, mainly because of the relatively lower mixing ratios associated with the Valtellina event.

c. Sensitivity to size distribution parameterizations

Switching to the modified size distribution parameterization has the largest effect on the model manifolds. Comparing the second rows of Figs. 6a–b with the third rows indicates that the measurement manifolds now better overlap all model manifolds, particularly the COHMEX and HURRICANE manifolds over land and the HURRICANE manifold over ocean. The model manifolds in the third rows differ from each other in terms of the associated liquid and ice mass contents, vertical distribution and mixing of hydrometeors, ice particle densities, and truncation limits of the size distribution functions. The variation of slope in the Marshall–Palmer size distribution has a strong impact on varying Mie optical properties of the hydrometeors, which leads to the main adjustments in shapes and positions of the associated model manifolds. The portions of the land and ocean measurement manifolds characterized by large 37-GHz TBs that never overlap the model manifolds originate from imperfect detection and screening of the raining SSM/I pixels, not problems intrinsic to the microphysical modeling.

The major changes in the modified size distribution parameterization occur for rain as well as for graupel

below the freezing level, for which we introduce the dependence on particle fall rate to calculate the size distribution parameters (see the appendix). Over land the CCOPE contours overlap those of the measurement manifold in the 37–85 GHz plane, but the 19-GHz TBs are still shifted toward lower values because of the weak emission from the rain layers. The impact of the small rain mass contents is stronger over ocean than over land with the CCOPE manifold exhibiting lower TBs at all frequencies.

Over land, the regions in the measurement manifold where the 85-GHz TBs are low ($<$170 K), are well matched in the 19–85 and 37–85 GHz planes for both the HURRICANE and COHMEX manifolds. These regions correspond to cloud structures with large mass contents of ice and graupel. The modified size distribution parameterization reduces the scattering effect at the lower frequencies and also reduces the correlation of 85 GHz with the lower frequencies, particularly with 19 GHz.

Over ocean, all contour shapes of the model manifolds in the third row change significantly with respect to those in the second row. The HURRICANE model manifold overlaps the measurement manifold much better than the COHMEX manifold, particularly in the 19–85 GHz plane. Both 37 and 85 GHz TBs reach lower values than the measurements because of the large mass of ice particles associated with the UW-NMS simulations. The over-ocean model manifold generated from the COHMEX simulation shows poorer overlap with the measurements but, as with the HURRICANE case, the changes obtained with the new size distribution parameterization are significant, particularly at 19 GHz. The reason that the measurement manifold of the Typhoon Oliver event does not extend down into the low TB tail, apparent in all three manifold planes, stems from the low concentration of ice particles characteristic of the convective systems in TOGA COARE (see Smith et al. 1996).

6. Impact of cloud–radiation databases on retrieval

The analysis carried out in the previous section demonstrates that microphysical parameterizations and environmental conditions of simulated storms are critical factors influencing the model manifolds. In essence, agreement with measurement manifolds can be achieved using model manifolds generated from different simulations. The purpose of this section is to show that a good overlapping of measurement and model manifolds does not guarantee the adequacy of a cloud–radiation database to represent an observed event. It is just as important to identify the typology of the observed cloud system and to associate it to an appropriate cloud-model simulation because the estimation of precipitation and cloud structures from profile-based retrieval algorithms is closely linked to the cloud–radiation database.

We use the modified over-land and over-ocean COHMEX and HURRICANE databases, that is, those obtained by modifying the meteorological profiles and size distribution parameterizations, for the retrieval of the two cases whose environmental profiles have been used to generate the databases. These consist of the Valtellina Flood and Typhoon Oliver events. In Figs. 7a–b we have illustrated the modified COHMEX and HURRICANE model manifolds, together with the measurement manifolds generated from the two selected cases. Rendered color graphics diagrams, incorporating the three-dimensional TB space defined by unpolarized brightness temperatures at 19, 37, and 85 GHz are used to portray the shape and overlap properties and to provide an overall view of the manifolds. Figure 7a shows the overland model manifolds and Valtellina Flood measurement manifold, while Fig. 7b shows the over-ocean model manifolds and Typhoon Oliver measurement manifold. In each diagram the manifolds are shown for two different perspective views. The overlap between the measurement and model manifolds is close, in particular over land (Fig. 7a), except for the mismatch in the region with the highest 37-GHz TBs, which stems from screening problems. Over ocean (Fig. 7b), the COHMEX manifold does not match the portion of the measurement manifold characterized by large TBs at 19 and 85 GHz. This mismatch arises because the COHMEX storm lacks any meaningful warm rain situations, characteristic of tropical cyclones.

In Figs. 8a–b we show retrieval results for both the Valtellina Flood and Typhoon Oliver events. In each diagram there are six panels indicating the correlation diagrams for columnar cloud, rain, graupel, pristine crystal, and snow/aggregate EWCs, as well as surface rain rate, between the mean retrievals obtained from the COHMEX database and the same from the HURRICANE database. The columnar snow and aggregate EWCs are combined for the COHMEX case. The columnar graupel EWCs retrieved with the two databases are very similar because this hydrometeor category has the largest impact on the upwelling TBs at all three frequencies. The columnar rain EWCs exhibit strong correlation for both ocean and land cases for columnar rain EWCs less than 3 kg m^{-2}, decreasing as the columnar path increases. This is particularly true for the land case. The better correlation for the ocean case stems from the different impact of rain-layer emission on the upwelling TBs, depending on surface emissivity conditions and on the magnitude of the columnar rain paths. Because of the strong correlation between the graupel retrievals for the two databases, nearly equivalent TBs across databases mean that the underlying emission sources are nearly equivalent. Over ocean, because surface emissivities are weak, equivalent emission requires equivalent columnar rain paths. Over land, since there is a significant emission source from the surface, equivalent emission does not necessarily require equivalent columnar rain paths.

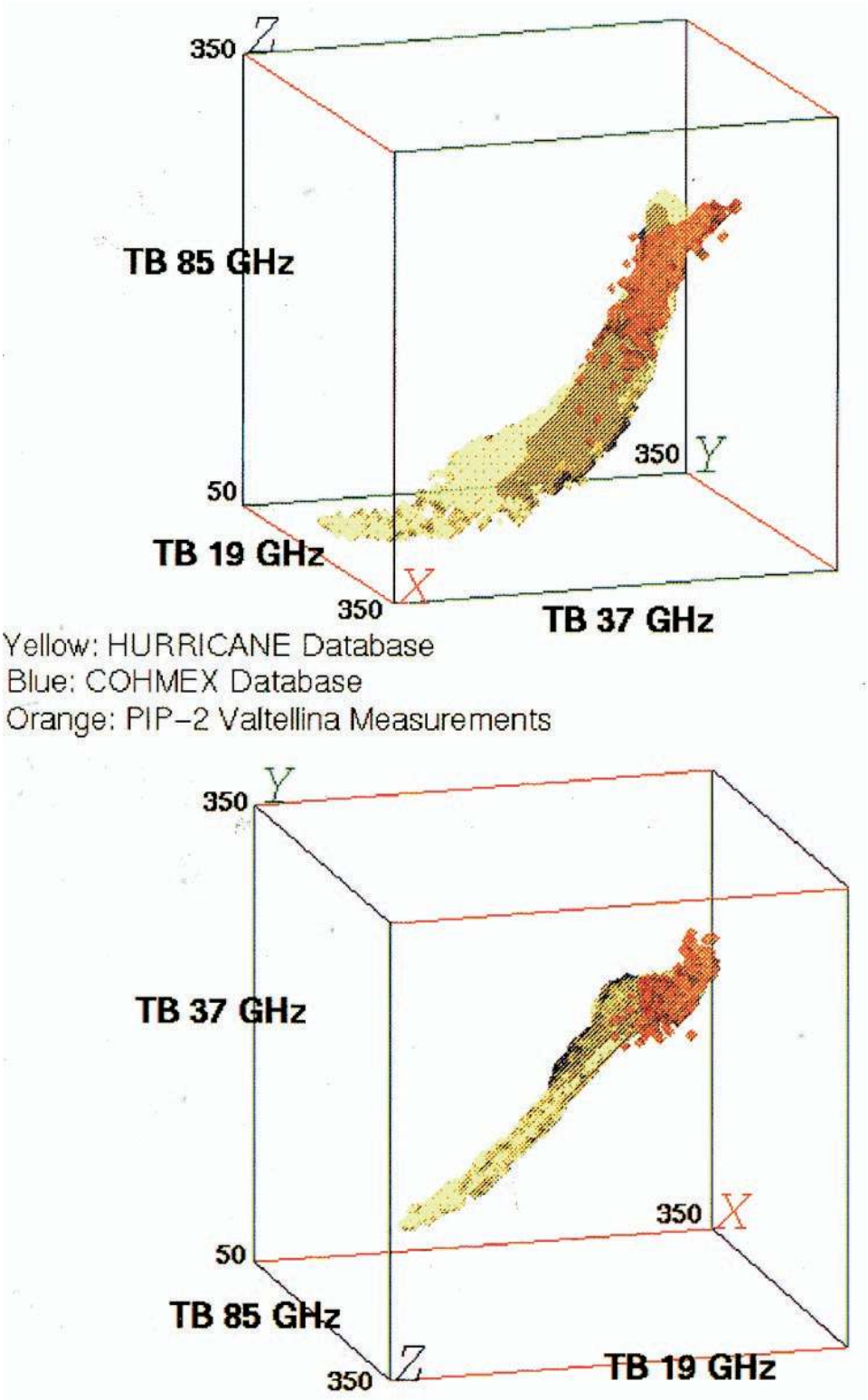

FIG. 7a. Color isosurfaces in 3D space of TBs in K at 19, 37, and 85 GHz, of the Valtellina Flood measurement manifold, and COHMEX and HURRICANE model manifolds calculated over land. The model manifolds are those obtained with the modified particle size distribution and the *T*–*q* profiles for the Valtellina event. Two different perspective views of the manifolds are given. The range limits of all axes are 50–350 K.

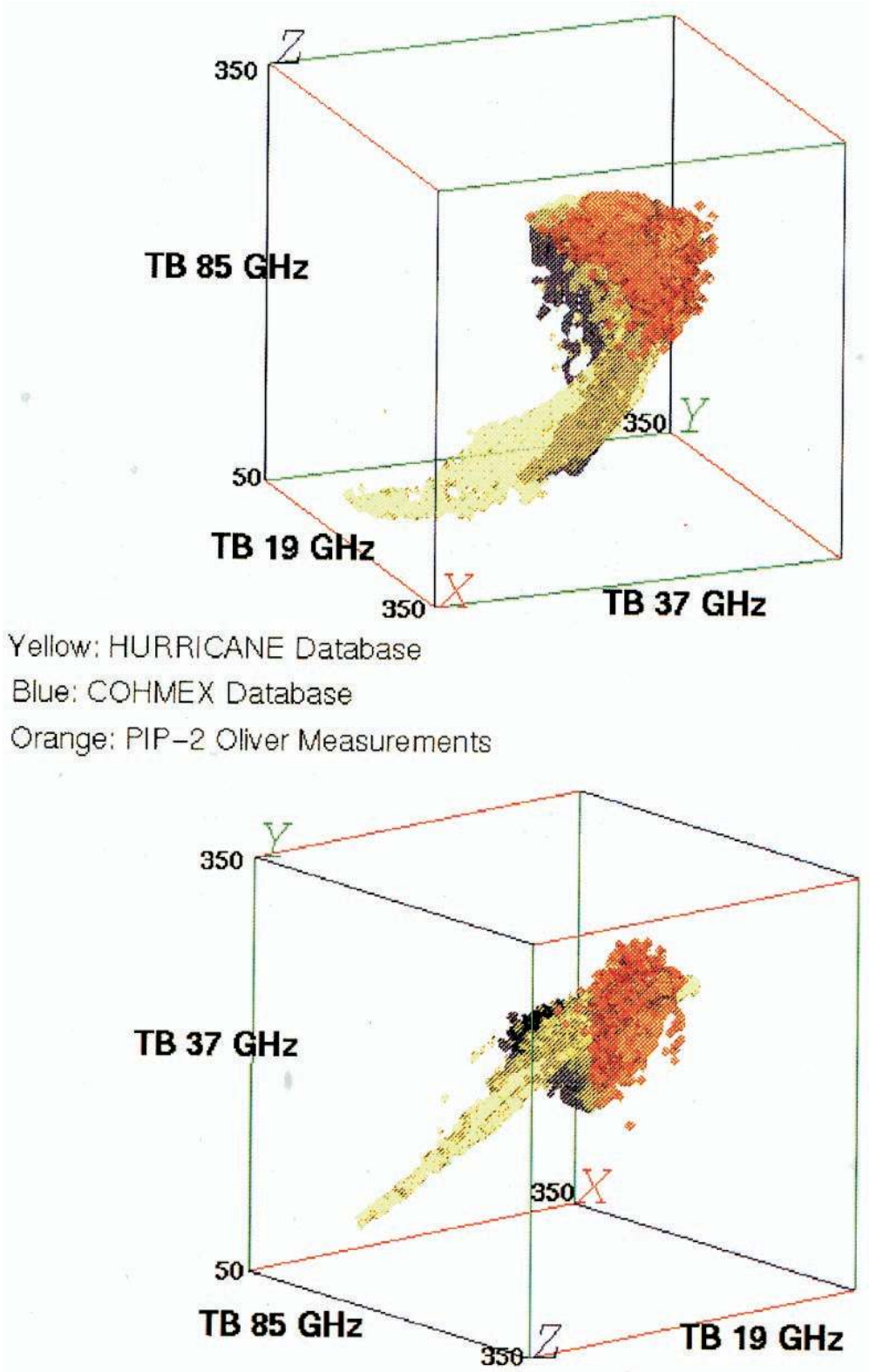

FIG. 7b. Same as (a) except for Typhoon Oliver measurement manifold, and for COHMEX and HURRICANE model manifolds calculated over ocean, using the *T–q* profiles for the Oliver event.

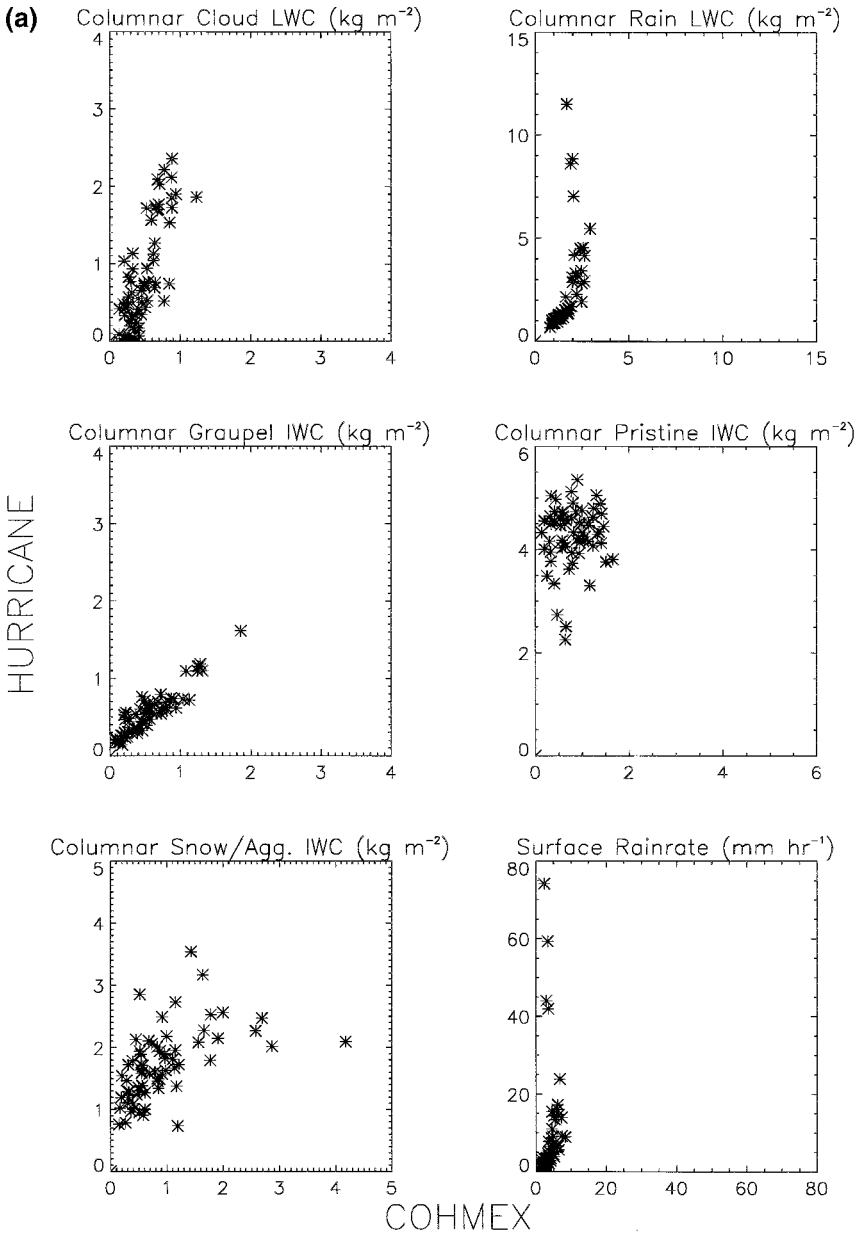

FIG. 8a. Correlation diagrams for columnar cloud, rain, graupel, pristine crystal, and snow/aggregate EWCs, along with surface rain rate, between mean retrievals for Valtellina case using modified COHMEX database (x axis) and mean retrievals using modified HURRICANE database (y axis).

The basic retrieval procedure for each point in the three-dimensional TB space of the measurement manifold consists of finding the points in each model manifold that are closest (in terms of Euclidean distance) to the measurements. Then the mean hydrometeor profiles in each database are obtained by averaging the cloud structures associated with the retrieved points. This requires that the retrieved cloud structures with the two databases are associated to nearly the same upwelling TBs. Yet, Figs. 8a–b indicate a lack of agreement between the other hydrometeor categories. For example, the columnar cloud EWCs retrieved with the HURRICANE database are larger than those retrieved with the COHMEX database. We believe this is because in the former case ice scattering produces a larger TB cooling at higher frequencies, thus requiring compensating TB warming due to a larger cloud water path. The very weak correlations for the pristine crystal and snow/aggregate categories arise from their negligible impact on the TBs. In general, the significant differences in the pristine crystal and snow/aggregate structures in the two databases have little impact on the retrievals.

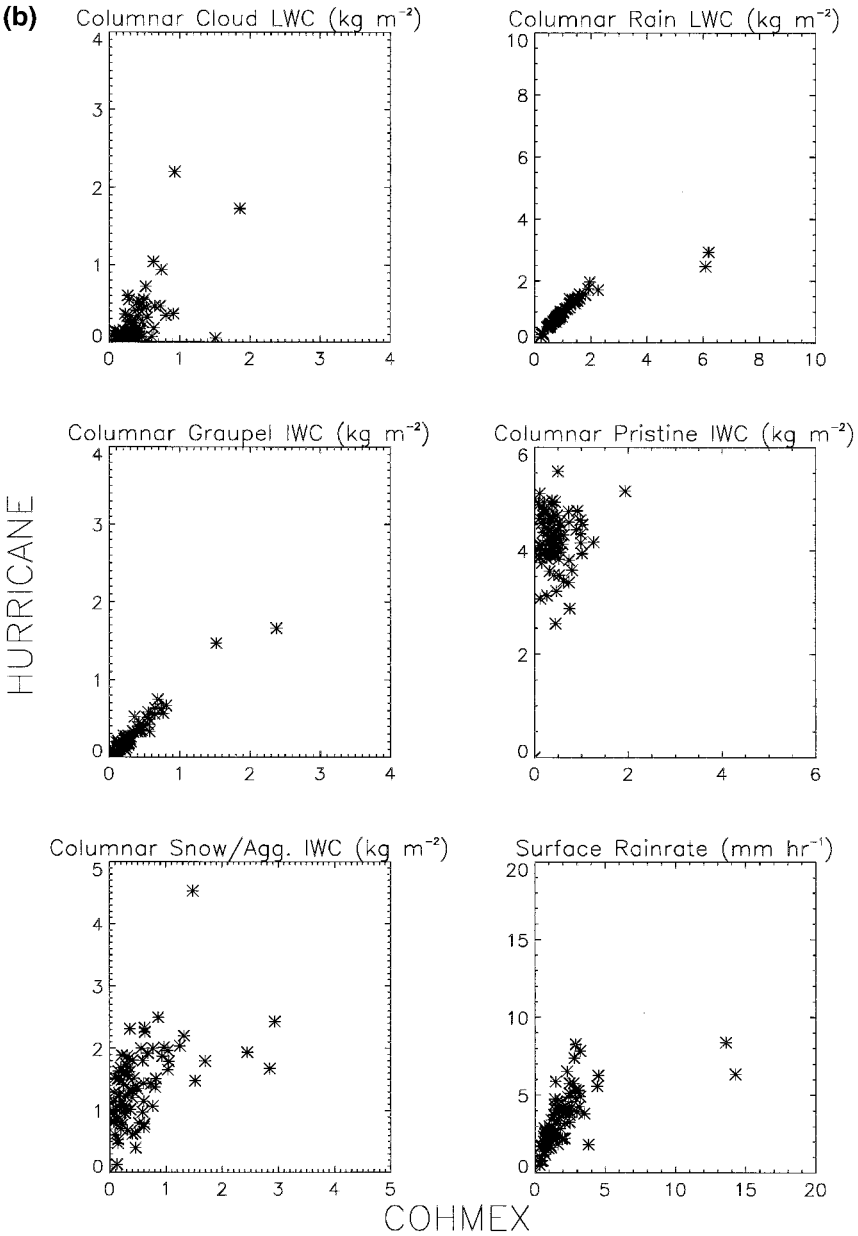

FIG. 8b. Same as (a) except for Typhoon Oliver case.

For both the Valtellina and Typhoon Oliver cases the surface rain rates retrieved using the HURRICANE database are larger than those retrieved with the COHMEX database. In the Oliver case, where there is an overall similarity of the columnar rain EWCs retrieved with the two databases, the surface rain rates estimated with the HURRICANE database are up to 2–3 times larger than found using the COHMEX database. Clearly the retrieved rain vertical structure can be quite different even when the columnar EWCs are very similar. This results from differences in the dynamical and microphysical features of the simulated events.

In order to analyze in detail the differences of the mean profiles retrieved with the two databases, their dispersion within the same database, and the subsequent uncertainties in precipitation retrieval we now focus on results obtained for just one pixel selected from each of the two PIP-2 cases. In Figs. 9a–b, we illustrate the mean hydrometeor EWC vertical profiles, and their standard deviations, for the selected pixels of the Valtellina Flood and Typhoon Oliver cases. The mean columnar EWCs of the various hydrometeors, the mean rain rates and their standard deviations, and the number of cloud structures retrieved for each pixel within a database are also indicated in each panel. The retrieved profiles for both selected cases exhibit different vertical structures

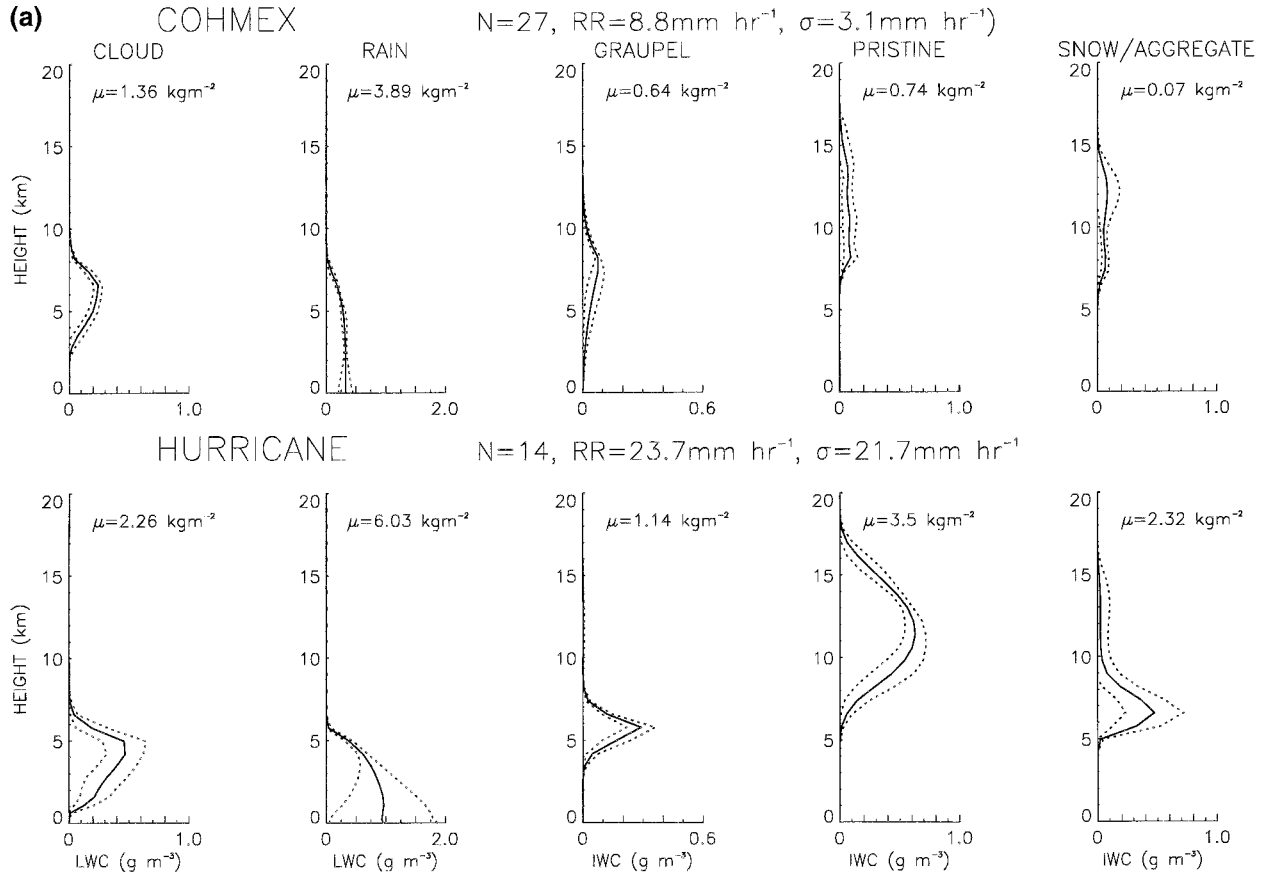

FIG. 9a. Mean hydrometeor EWC vertical profiles (along with ±1 standard deviation profiles), retrieved for one pixel selected from Valtellina Flood case using modified COHMEX database (top panels) and modified HURRICANE database (bottom panels). *N* is the number of cloud profiles retrieved within each database, RR is the average rain rate, σ is the rain-rate standard deviation, and μ is the average columnar LWC or IWC of the hydrometeor in each panel.

depending on whether the COHMEX or HURRICANE database was used. In the HURRICANE databases, the rain masses are concentrated below 5 km, while in the COHMEX databases they reach 8 km. Graupel has a very different profile. In the COHMEX cases it penetrates to levels close to the surface (unlike what is actually found in Pacific cyclones), while in the HURRICANE cases large concentrations are all above 3 km. The large differences in the mean profiles and the columnar rain mass contents and surface rain rates retrieved for the Valtellina case using the COHMEX and HURRICANE databases, particularly significant for rain and graupel, show that retrieval over land is more sensitive to the selected database. Moreover, the variances of the graupel and rain mean vertical profiles are larger for the Valtellina case than for the Oliver case, indicating greater uncertainties for land-based retrieval. Note that the warm rain properties of the HURRICANE database lead to the largest uncertainties. The differences in retrieved rain rates between the two databases demonstrate the sensitivity of precipitation retrieval to the detailed microphysical features of the simulations.

The main point of these results is that the dispersion in surface rain rates and cloud profiles are significant over rather negligible variations in the TBs and illustrates the underlying nonuniqueness problem with precipitation retrieval, even using multiple frequencies. This suggests that one should resort to less deterministic approaches than those presently used because profiles very close in terms of TB signatures can generate very different surface rain results. Rain-map algorithms are also vulnerable to these uncertainties but less well equipped to address them.

7. Discussion and conclusions

One of the main problems in the application of physically based precipitation profile retrieval algorithms based on the use of cloud–radiation databases is the mismatch between the TB domain populated by the cloud–radiation model and the TB domain populated by the measurements. In this study we have explored some of the main factors that contribute to this mismatch and have studied the sensitivity of rain-rate retrieval to properties of the cloud–radiation database used in the retrieval algorithm.

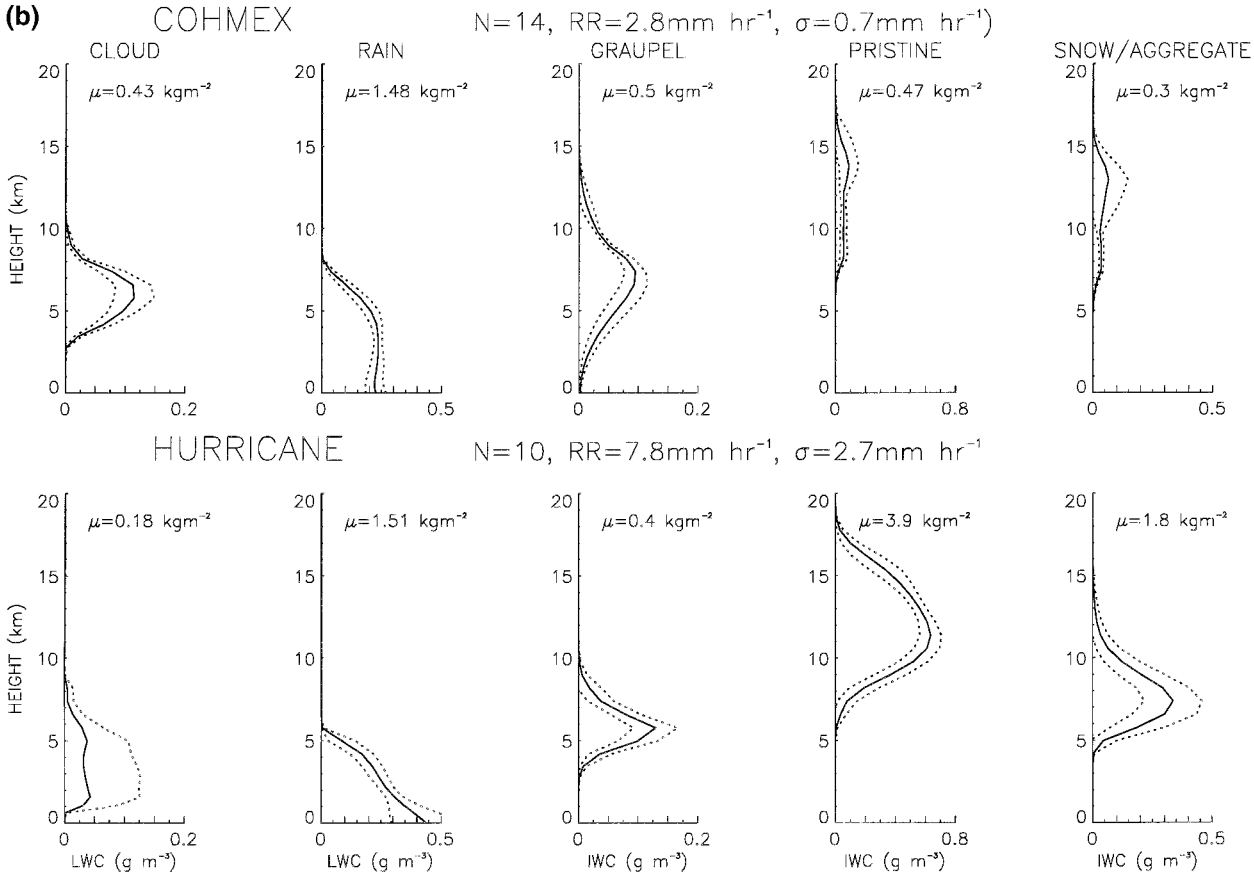

FIG. 9b. Same as (a) except for Typhoon Oliver case.

We have considered cloud–radiation databases generated from three different storm simulations: a Caribbean hurricane and a severe continental summer thunderstorm, carried out with the UW-NMS, along with a severe continental summer hailstorm, carried out with the WISCDYMM. The original cloud-model outputs have been averaged over a 10×10 km^2 grid mesh in order to obtain horizontally homogeneous cloud structures consistent with the highest-resolution SSM/I measurements. Then a selection procedure has been used to eliminate the redundancy of similar cloud structures. Finally, upwelling TBs at 19, 37, and 85 GHz have been calculated by imposing ocean or land surface emissivity conditions consistent with the simulated storm environment. Two measurement databases have been generated, one over land and one over ocean, using SSM/I measurements from selected cases of the PIP-2 study.

After analyzing the main microphysical, macrophysical, and environmental features of the three different storm simulations, we have related them to differences between the TB domains associated with each of the simulations. In particular, we have pointed out correlation differences among the three simulations between the TBs and the cloud constituents. The correlations between TBs and rain rates are larger for cold rain systems than warm rain systems because of the intrinsic correlation between rain and graupel, the latter being directly sensed. In the warm rain case, the TB–rain rate correlations are weaker because the SSM/I frequencies are not low enough to detect rain layers close to the surface. However, it is important to recognize that the correlation between ice content and surface rain rate is reduced for each of the three simulations in going to spatial resolutions higher than 10×10 km^2 because the effects of vertical shear become more enhanced. For example, the smallest ice content–surface rain-rate correlation is found in the high-resolution tropical cyclone simulation because this case contains both warm rain effects and shear-induced decoupling of ice layers and surface rain layers. In transforming to low resolution, the averaging of the cloud structures serves to filter out the most intense profiles and increases the intercorrelation between the ice content and surface rain rate, as well as the intercorrelations between ice, rain, and the TBs. This effect is particularly evident for the two small-scale continental storms, where the 10×10 km^2 grid-scale used to average hydrometeor profiles filters the effects of the horizontal transports.

The partial or total mismatches between model and measurement databases, and the large differences be-

tween the model databases themselves, are found to be related to characteristics of the simulated storms (environmental conditions, vertical distribution and mixing of hydrometeors, space–time scales) and to the cloud-model microphysical parameterizations, particularly hydrometeor size distribution. We have carried out sensitivity studies that estimate the individual impacts of the environmental factors and the size distribution parameterizations on the TBs and have sought means to overcome mismatches between model and measurement databases. The impact of environmental conditions, that is, moisture and temperature profiles, are significant for the over-land databases (changes in TBs up to 10 K) and very significant for over-ocean databases, where TBs at all frequencies can vary up to 40 K.

The largest changes in the boundaries and densities of the model manifolds occur when a Marshall–Palmer size distribution parameterization different from that assumed in the model is introduced for rain, graupel, snow, and aggregates. For the UW-NMS and WISCDYMM, this means allowing both the slope and intercept of the particle size distribution function to vary according to atmospheric temperature and mean particle fall rate at each vertical level. The variation of slope has strong impact by decreasing the scattering effects of ice particles at low frequencies, in particular by graupel particles, because the change to a variable slope formulation effectively reduces the mass of large ice particles. As a consequence, the correlations of the TBs at 19 GHz with the columnar masses of graupel, which were large in the original databases, become weak in the modified databases (in particular for the UW-NMS simulations) and, at the same time, the TBs at 19 and 37 GHz increase. The CCOPE simulation shows a significant decrease of TBs at 85 GHz because of the increase in concentration of small graupel particles with respect to the original size distribution. A good matchup with the measurements is achieved for the UW-NMS simulations, while the hailstorm simulation, characterized by relatively low rainwater contents, exhibits lower TBs because of the relatively lower rain layer emission.

In order to study the sensitivity of the retrievals to the cloud–radiation databases, we have used the two databases generated from the UW-NMS simulations that match closely to the measurements. In so doing, we have selected two PIP-2 events from those used to generate the measurement manifolds, one over land and one over ocean. The microphysical details of the simulated storms strongly influence the retrieval results. First of all, the columnar mass contents of the various hydrometeors retrieved using different databases can be very different. Second, even when the retrieved columnar rain mass contents are identical, retrieved surface rain rate differences can exceed a factor of 2 because of differences in the retrieved rain vertical profile. Finally, when using an Euclidean distance retrieval scheme within a single database, the retrieved cloud structures and rain rates for a given pixel can be widely dispersed. Although dispersion is not so serious with the continental thunderstorm simulation in which the ice phase dominates, in the case of the tropical cyclone simulation, warm rain situations produce strong dispersion effects. The effects are amplified over a land background where the surface rain layers are even less influential on the upwelling TBs.

In order to have good fidelity in the retrieval of both surface rain rates and hydrometeor profile structures, it is important to have strong internal correlation between the cloud constituents, not all of which are directly sensed by the radiometer. This is particularly true for the over-land case where the contrast between the rain layers and the surface is poor. However, a good matchup between the measurement and model manifolds does not guarantee that a single cloud–radiation database is appropriate for a given measurement. We submit that it is important to identify the typology of an observed event and to associate it with the appropriate cloud–radiation database, generated from a simulation that adequately reproduces the microphysical, macrophysical, and environmental features of the storm.

In the future, physical inversion profile retrieval schemes will sustain some improvement as the spatial resolution of the measurements improve and as lower-frequency channels are included with the radiometers. Although there will be some problems associated with taking advantage of higher-resolution measurements, because of the effect of vertical shear decoupling, less blurred renditions of storm features will aid physical inversion techniques. The use of lower frequencies will provide direct information on the entire precipitating column. This is particularly useful over an ocean background due to the high contrast between the cold ocean brightness temperatures and warm precipitation emission temperatures observable at such low frequencies. The potential improvement in characterization of rainfall processes by going to high-resolution measurements and to lower more penetrating frequencies has been explored by Marzano et al. (1994) and Smith et al. (1994c). Significant improvements in precipitation retrieval should take place after launch of the low earth orbit Tropical Rainfall Measuring Mission satellite, which will use a passive microwave imager similar to the SSM/I but with the addition of a polarized 10.7-GHz channel (Simpson et al. 1996).

As a final note, it is important to recognize that physical profile inversion schemes are limited by their dependence on the weaknesses and approximations of the cloud models in replicating the physics, dynamics, and microphysics of precipitating storms. The 1D radiative transfer models currently used in published retrieval algorithms are another source of weakness. Clearly improvements in cloud models and their physical parameterizations will overcome some of the limitations in physically based inversion algorithms. But, at the same time, the development of three-dimensional radiative transfer models that account for the horizontal and ver-

tical variability of rain features will ultimately be needed to optimally represent the sensitivity of precipitation retrieval to the microphysical details of particle size distribution and shape.

Acknowledgments. The authors express their appreciation to Barbara Burns for her helpful comments on the cloud-radiation database properties, to Dan Johnson for his advice on the microphysical parameterization of the WISCDYMM, and to Pete Pokrandt for his help in executing the UW-NMS simulations. SSM/I data have been provided by NASA's WetNet Project directed by Jim Dodge. This research has been supported by Gruppo Nazionale per la Difesa dalle Catastrofi Idrogeologiche, Agenzia Spaziale Italiana, European Space Agency ESA-ESTEC Purchase Orders 142042 and 152545, and Commission of European Communities, Environment and Climate Programme 1996–1999 (Contract ENV4-CT96-0281). NATO Travel Grant CG-890894 provided essential travel support. Gregory Tripoli has been supported by NSF Grant ATM-9520606, Pao Wang by NSF Grant ATM 9314465, and Eric Smith and Xuwu Xiang by NASA Grants NAGW-3970 and NAG5-2672. A portion of the computer resources has been provided by the Supercomputer Computations Research Institute at the Florida State University under U.S. Department of Energy Contract DOE-FCO585ER250000.

APPENDIX

Modified Size Distribution Parameterization

Here we give the details of the procedure followed to vary the model size-distribution parameterization of rain, graupel, snow, and aggregates. The EWC (l_h) at each vertical level for each hydrometeor category, with a size distribution function $n(D)$, is given by

$$l_h = \frac{4}{3}\pi \int_0^\infty \left(\frac{D}{2}\right)^3 \rho_h n(D)\, dD, \tag{A1}$$

where ρ_h is the particle density. Assuming the Marshall–Palmer size distribution function given in Eq. (1), we have

$$B = \left(\frac{\pi \rho_h A}{l_h}\right)^{1/4}. \tag{A2}$$

For graupel, snow, and aggregates we have considered the formulation given by Straka (1989) that relates the intercept A to the atmospheric temperature at each level and accounts for the general observation that there are more and smaller particles at colder temperatures and fewer at warmer temperatures. We have

$$A = A_0 \exp[a(T - T_0)], \tag{A3}$$

where T is the atmospheric temperature and T_0 is 273.16 K. Here A_0 and a are specified for each hydrometeor category (a changes above or below the freezing level); their values are given in Table A1. Combining Eq. (A3) with Eq. (A2), we obtain the slope B.

For rain and graupel located below the freezing level, we have considered the dependence of the intercept A on the particle mean precipitation rate (RR) at a given height level according to Pruppacher and Klett (1988) and Ludlam (1994). For graupel, this relationship is used within Eq. (A3). Thus, the general formulation is

$$A = A_1 \mathrm{RR}^k \exp[a(T - T_0)], \tag{A4}$$

where (RR) is in mm h^{-1}, while A_1, k, and a are given in Table A1. Here RR is related to the slope B if we assume that the raindrops and the graupel particles of diameter D have a particle fall speed v_d given by the power law

$$v_d = \alpha D^\beta. \tag{A5}$$

Thus, combining Eq. (A1) with the definition of precipitation rate

$$\mathrm{RR} = \frac{\pi}{6} \int_0^\infty v_d D^3 n(D)\, dD, \tag{A6}$$

we obtain

$$\mathrm{RR} = \frac{\alpha \Gamma(4 + \beta)}{6B^\beta} \frac{l_h}{\rho_h}. \tag{A7}$$

This simplifies to

$$\mathrm{RR} = k_0 \frac{V_\infty}{\rho_h} l_h, \tag{A8}$$

where the mass-weighted mean terminal velocity is given by

$$V_\infty = \frac{\alpha \Gamma(4 + \beta)}{6B^\beta}, \tag{A9}$$

with V_∞ (in m s^{-1}) ρ_h and l_h (in kg m^{-3}), and k_0 set to

TABLE A1. Constant values used for the slope and intercept calculations of the modified size distribution. They are specified for atmospheric temperatures below and above the freezing temperature T_0 = 273.16 K.

	A_0 (m^{-4})	A_1 (m^{-4} mm^{-k} h^k)	a (K^{-1})	k
Rain		7×10^6	0	0.37
Graupel	4×10^6 ($T < T_0$)	6.52×10^2 ($T > T_0$)	-2.5×10^{-2} ($T < T_0$) -7.5×10^{-2} ($T > T_0$)	0 ($T < T_0$) 0.872 ($T > T_0$)
Snow/aggregates	4×10^6 ($T < T_0$) 4×10^6 ($T > T_0$)		-3.8×10^{-2} ($T < T_0$) -8.8×10^{-2} ($T > T_0$)	0 0

3.6×10^6 to convert RR to millimeters per hour. α and β have been taken from Straka (1989); for rain we have β equal to 0.8 and

$$\alpha = 21.15\left(\frac{\rho_0}{\rho_a}\right)^{0.5} \quad [\mathrm{m}^{1-\beta}\ \mathrm{s}^{-1}], \tag{A10}$$

where ρ_0 is the air density at 1000 mb and ρ_a is the air density at each level. For graupel we have β equal to 0.5 and

$$\alpha = \left(\frac{4g\rho_h}{3C_D\rho_a}\right)^{0.5} \quad [\mathrm{m}^{1-\beta}\ \mathrm{s}^{-1}], \tag{A11}$$

where g is 9.8 m s^{-2} and C_D is the drag coefficient, assumed to be 0.6.

Combining Eqs. (A2), (A4), (A8), and (A9) we have

$$B = \left[\frac{\rho_h \pi A_2}{l_h}\left(k_0 \frac{l_h}{\rho_h}\alpha \frac{\Gamma(4+\beta)}{6}\right)^k\right]^{1/(4+\beta k)}, \tag{A12}$$

where

$$A_2 = A_1 \exp[a(T - T_0)]. \tag{A13}$$

Combining Eq. (A9) with Eq. (A8), we obtain the precipitation rate RR at each level. Then, from Eq. (A4), we obtain A.

In order to account for the radius truncation limits assumed for the various hydrometeor categories, we have introduced a renormalization factor in the calculation of A. The equivalent water content l_h, given by Eq. (A1), becomes

$$l_h = \frac{4}{3}\pi A' \int_{r_1}^{r_2} \exp(-B'r) r^3 \rho_h(r)\, dr \tag{A14}$$

or

$$l_h = \frac{4}{3}\pi A' B'^{-4} \int_{Br_1}^{Br_2} \exp(-s) s^3 \rho_h(s)\, ds, \tag{A15}$$

where $A' = 2A$, $B' = 2B$, $s = B'r$, and r_1 and r_2 are the radius truncation limits given in Table 3. When the density ρ_h is constant, the result of the integral is

$$\begin{aligned} I_1 = {} & \exp(-B'r_1)[(B'r_1)^3 + 3(B'r_1)^2 + 6(B'r_1) + 6] \\ & - \exp(-B'r_2)[(B'r_2)^3 + 3(B'r_2)^2 + 6(B'r_2) + 6], \end{aligned}$$

while for snow and aggregates in the COHMEX and HURRICANE simulations, where the density ρ varies according to Eq. (3), the integral is

$$\begin{aligned} I_2 &= \int_{Br_1}^{Br_2} s^{2.4} \exp(-s)\, ds \\ &= \gamma(3.4, B'r_2) - \gamma(3.4, B'r_1), \end{aligned} \tag{A17}$$

where γ is the incomplete gamma function.

REFERENCES

Cotton, W. R., M. A. Stephens, T. NehrKorn, and G. J. Tripoli, 1982: The Colorado State University three-dimensional cloud/mesoscale model. Part II: An ice phase parameterization. *J. Rech. Atmos.,* **16,** 295–320.

——, G. J. Tripoli, R. M. Rauber, and E. A. Mulvihill, 1986: Numerical simulation of the effects of varying ice crystal nucleation rate and aggregation processes on orographic snowfall. *J. Climate Appl. Meteor.,* **25,** 1658–1680.

Evans, K. F., J. Turk, T. Wong, and G. L. Stephens, 1995: A Bayesian approach to microwave precipitation profile retrieval. *J. Appl. Meteor.,* **34,** 260–279.

Farrar, M. R., and E. A. Smith, 1992: Spatial resolution enhancement of terrestrial features using deconvolved SSM/I microwave brightness temperatures. *IEEE Trans. Geosci. Remote Sens.,* **2,** 349–355.

——, ——, and X. Xiang, 1994: The impact of spatial resolution enhancement of SSM/I microwave brightness temperature on rainfall retrieval algorithm. *J. Appl. Meteor.,* **33,** 313–333.

Ferraro, R. R., E. A. Smith, W. Berg, and G. J. Huffman, 1998: A screening methodology for passive microwave precipitation retrieval algorithms. *J. Atmos. Sci.,* **55,** 1583–1600.

Flatau, P., G. J. Tripoli, J. Berlinder, and W. Cotton, 1989: The CSU-RAMS cloud microphysics module: General theory and code documentation. Atmospheric Sciences Rep. 451, 88 pp. [Available from Colorado State University, Fort Collins, CO 80523.]

Haferman, J. L., W. F. Krajewski, and T. F. Smith, 1994: Three-dimensional aspects of radiative transfer in remote sensing of precipitation: Application to the 1986 COHMEX storm. *J. Appl. Meteor.,* **33,** 1609–1622.

Johnson, D. E., P. K. Wang, and J. M. Straka, 1993: Numerical simulation of the 2 August 1981 CCOPE supercell storm with and without ice microphysics. *J. Appl. Meteor.,* **32,** 745–759.

——, ——, and ——, 1994: A study of microphysical process in the 2 August 1981 CCOPE supercell storm. *Atmos. Res.,* **33,** 93–123.

Kanak, K. M., 1990: Three-dimensional, non-hydrostatic, numerical simulation of a developing tropical cyclone. M.S. thesis, Dept. of Atmospheric and Oceanic Sciences, University of Wisconsin—Madison, 130 pp. [Available from Dept. of Atmospheric and Oceanic Sciences, University of Wisconsin—Madison, Madison, WI 53706.]

Kummerow, C., and L. Giglio, 1994a: A passive microwave technique for estimating rainfall and vertical structure information from space. Part I: Algorithm description. *J. Appl. Meteor.,* **33,** 3–18.

——, and ——, 1994b: A passive microwave technique for estimating rainfall and vertical structure information from space. Part II: Applications to SSM/I data. *J. Appl. Meteor.,* **33,** 19–34.

Liebe, H. J., 1985: An updated model for millimeter wave propagation in moist air. *Radio Sci.,* **20,** 1069–1089.

——, and G. G. Gimmestad, 1978: Calculation of clear air EHF refractivity. *Radio Sci.,* **13,** 245–251.

Lin, Y. L., R. D. Farley, and H. D. Orville, 1983: Bulk parameterization of the snow field in a cloud model. *J. Climate Appl. Meteor.,* **22,** 1065–1092.

Ludlam, F. H., 1994: *Clouds and Storms: The Behavior and Effect of Water in the Atmosphere.* The Pennsylvania State University Press, 405 pp.

Marzano, F. S., A. Mugnai, E. A. Smith, X. Xiang, J. Turk, and J. Vivekanandan, 1994: Active and passive remote sensing of precipitating storms during CaPE. Part II: Intercomparison of precipitation retrievals over land from AMPR radiometer and CP-2 radar. *Meteor. Atmos. Phys.,* **54,** 29–51.

Mugnai, A., and E. A. Smith, 1988: Radiative transfer to space through a precipitating cloud at multiple microwave frequencies. Part I: Model description. *J. Appl. Meteor.,* **27,** 1055–1073.

——, H. J. Cooper, E. A. Smith, and G. J. Tripoli, 1990: Simulation of microwave brightness temperatures of an evolving hail storm at SSM/I frequencies. *Bull. Amer. Meteor. Soc.,* **71,** 2–13.

——, E. A. Smith, and G. J. Tripoli, 1993: Foundations for statistical–physical precipitation retrieval from passive microwave satellite measurements. Part II: Emission source and generalized weighting function properties of a time-dependent cloud–radiation model. *J. Appl. Meteor.,* **32,** 17–39.

——, F. S. Marzano, and N. Pierdicca, 1994: Precipitation retrieval from spaceborne microwave radiometers: Description and application of a maximum likelihood profile algorithm. *Proc. CLIMPARA'94: Climatic Parameters in Radiowave Propagation Prediction,* Moscow, Russia, International Union of Radio Science, 2.2.1–2.2.4.

Panegrossi, G., S. Dietrich, F. S. Marzano, and A. Mugnai, 1996: Study on the use of cloud-radiation models for passive microwave precipitation retrieval. IF A Internal Rep. 13-96, 104 pp. [Available from Istituto di Fisica dell'Atmosfera, Consiglio Nazionale delle Ricerche, P.le Sturzo 31, 00144 Rome, Italy.]

Petty, G. W., and K. Katsaros, 1994: The response of the SSM/I to the marine environment. Part II: A parameterization of the effect of the sea surface slope distribution on emission and reflection. *J. Atmos. Oceanic Technol.,* **11,** 617–628.

Pielke, R. A., W. R. Cotton, R. L. Walko, W. A. Lyons, L. D. Grasso, M. E. Nicholls, M. D. Moran, D. A. Wesley, T. J. Lee, and J. H. Copeland, 1992: A comprehensive meteorological modeling system. *Meteor. Atmos. Phys.,* **49,** 69–91.

Pierdicca, N., F. S Marzano, P. Basili, P. Ciotti, G. d'Auria, and A. Mugnai, 1996: Precipitation retrieval from spaceborne microwave radiometers based on multivariate analysis of simulated cloud-radiation datasets. *IEEE Trans. Geosci. Remote Sens.,* **34,** 1–16.

Pruppacher, H. R., and J. D. Klett, 1978: *Microphysics of Clouds and Precipitation.* D. Reidel, 714 pp.

Roberti, L., J. L. Haferman, and C. Kummerow, 1994: Microwave radiative transfer through horizontally inhomogeneous precipitating clouds. *J. Geophys. Res.,* **99,** 16 707–16 718.

Simpson, J., C. Kummerow, W. K. Tao, and R. F. Adler, 1996: On the Tropical Rainfall Measuring Mission (TRMM) satellite. *Meteor. Atmos. Phys.,* **60,** 19–36.

Smith, E. A., and A. Mugnai, 1988: Radiative transfer to space through a precipitating cloud at multiple microwave frequencies. Part II: Results and analysis. *J. Appl. Meteor.,* **27,** 1074–1091.

——, ——, H. J. Cooper, G. J. Tripoli, and X. Xiang, 1992: Foundations for statistical–physical precipitation retrieval from passive microwave satellite measurements. Part I: Brightness-temperature properties of a time-dependent cloud–radiation model. *J. Appl. Meteor.,* **31,** 506–531.

——, C. Kummerow, and A. Mugnai, 1994a: The emergence of inversion-type profile algorithms for estimation of precipitation from satellite passive microwave measurements. *Remote Sens. Rev.,* **11,** 211–242.

——, X. Xiang, A. Mugnai, and G. J. Tripoli, 1994b: Design of an inversion-based precipitation profile retrieval algorithm using an explicit cloud model for initial guess microphysics. *Meteor. Atmos. Phys.,* **54,** 53–78.

——, ——, ——, R. Hood, and R. W. Spencer, 1994c: Behavior of an inversion-based precipitation retrieval algorithm with high-resolution AMPR measurements including a low-frequency 10.7-GHz channel. *J. Atmos. Oceanic Technol.,* **11,** 858–873.

——, A. Mugnai, and G. J. Tripoli, 1995: Theoretical foundations and verification of a multispectral, inversion-type microwave precipitation profile retrieval algorithm. *Passive Microwave Remote Sensing of Land-Atmosphere Interactions,* VSP Press, 599–621.

——, J. Turk, M. Farrar, A. Mugnai, and X. Xiang, 1996: Estimating 13.8-GHz path-integrated attenuation from 10.7-GHz brightness temperatures for TRMM combined PR–TMI precipitation algorithm. *J. Appl. Meteor.,* **36,** 365–388.

——, L. Lamm, R. Adler, J. Alishouse, K. Aonashi, E. Barrett, P. Bauer, W. Berg, A. Chang, R. Ferraro, J. Ferriday, S. Goodman, N. Grody, C. Kidd, D. Knireton, C. Kummerow, G. Liu, F. Marzano, A. Mugnai, W. Olson, G. Petty, A. Shibata, R. Spencer, F. Wentz, T. Wilheit, and E. Zipser, 1998. Results of WetNet 1997: PIP-2 project. *J. Atmos. Sci.,* **55,** 1483–1536.

Spencer, R. W., R. E Hood, F. J. LaFontaine, E. A Smith, J. Galliano, and E. Lobl, 1994: High-resolution imaging of rain systems with the advanced microwave precipitation radiometer. *J. Atmos. Oceanic Technol.,* **11,** 849–857.

Straka, J. M., 1989: Hail growth in a highly glaciated central high plains multi-cellular hailstorm. Ph.D. dissertation, University of Wisconsin—Madison, 413 pp. [Available from Dept. of Atmospheric and Oceanic Sciences, University of Wisconsin—Madison, Madison, WI 53706.]

Tripoli, G. J., 1992a: A nonhydrostatic model designed to simulate scale interaction. *Mon. Wea. Rev.,* **120,** 1342–1359.

——, 1992b: An explicit three-dimensional nonhydrostatic numerical simulation of a tropical cyclone. *Meteor. Atmos. Phys.,* **49,** 229–254.

——, and W. R. Cotton, 1982: The Colorado State University three-dimensional cloud/mesoscale model—1982. Part I: General theoretical framework and sensitivity experiments. *J. Rech. Atmos.,* **16,** 185–200.

——, and ——, 1986: An intense, quasi-steady thunderstorm over mountainous terrain. Part IV: Three-dimensional numerical simulation. *J. Atmos. Sci.,* **43,** 894–912.

——, and ——, 1989: Numerical study of an observed orogenic mesoscale convective system. Part I: Simulated genesis and comparison with observations. *Mon. Wea. Rev.,* **117,** 273–304.

Wilheit, T. T., R. Adler, S. Avery, E. C. Barrett, P. Bauer, W. Berg, A. Chang, J. Ferriday, N. Grody, S. Goodman, C. Kidd, D. Kniveton, C. Kummerow, A. Mugnai, W. Olson, G. Petty, A. Shibata, E. A. Smith, and R. W. Spencer, 1994: Algorithms for the retrieval of rainfall from passive microwave measurements. *Remote Sens. Rev.,* **11,** 163–194.

Xiang, X., E. A. Smith, and C. G. Justus, 1994: A rapid radiative transfer model for reflection of solar radiation. *J. Atmos. Sci.,* **51,** 1978–1988.